PHYSICAL REVIEW D **94,** 092004 (2016)

Measurement of the inclusive $t\bar{t}$ production cross section in $p\bar{p}$ collisions at $\sqrt{s}=1.96$ TeV and determination of the top quark pole mass

V. M. Abazov,[31] B. Abbott,[67] B. S. Acharya,[25] M. Adams,[46] T. Adams,[44] J. P. Agnew,[41] G. D. Alexeev,[31] G. Alkhazov,[35] A. Alton,[56,a] A. Askew,[44] S. Atkins,[54] K. Augsten,[7] Y. Aushev,[38] C. Avila,[5] F. Badaud,[10] L. Bagby,[45] B. Baldin,[45] D. V. Bandurin,[73] S. Banerjee,[25] E. Barberis,[55] P. Baringer,[53] J. F. Bartlett,[45] U. Bassler,[15] V. Bazterra,[46] A. Bean,[53] M. Begalli,[2] L. Bellantoni,[45] S. B. Beri,[23] G. Bernardi,[14] R. Bernhard,[19] I. Bertram,[39] M. Besançon,[15] R. Beuselinck,[40] P. C. Bhat,[45] S. Bhatia,[58] V. Bhatnagar,[23] G. Blazey,[47] S. Blessing,[44] K. Bloom,[59] A. Boehnlein,[45] D. Boline,[64] E. E. Boos,[33] G. Borissov,[39] M. Borysova,[38,l] A. Brandt,[70] O. Brandt,[20] R. Brock,[57] A. Bross,[45] D. Brown,[14] X. B. Bu,[45] M. Buehler,[45] V. Buescher,[21] V. Bunichev,[33] S. Burdin,[39,b] C. P. Buszello,[37] E. Camacho-Pérez,[28] B. C. K. Casey,[45] H. Castilla-Valdez,[28] S. Caughron,[57] S. Chakrabarti,[64] K. M. Chan,[51] A. Chandra,[72] E. Chapon,[15] G. Chen,[53] S. W. Cho,[27] S. Choi,[27] B. Choudhary,[24] S. Cihangir,[45] D. Claes,[59] J. Clutter,[53] M. Cooke,[45,k] W. E. Cooper,[45] M. Corcoran,[72] F. Couderc,[15] M.-C. Cousinou,[12] J. Cuth,[21] D. Cutts,[69] A. Das,[71] G. Davies,[40] S. J. de Jong,[29,30] E. De La Cruz-Burelo,[28] F. Déliot,[15] R. Demina,[63] D. Denisov,[45] S. P. Denisov,[34] S. Desai,[45] C. Deterre,[41,c] K. DeVaughan,[59] H. T. Diehl,[45] M. Diesburg,[45] P. F. Ding,[41] A. Dominguez,[59] A. Dubey,[24] L. V. Dudko,[33] A. Duperrin,[12] S. Dutt,[23] M. Eads,[47] D. Edmunds,[57] J. Ellison,[43] V. D. Elvira,[45] Y. Enari,[14] H. Evans,[49] A. Evdokimov,[46] V. N. Evdokimov,[34] A. Fauré,[15] L. Feng,[47] T. Ferbel,[63] F. Fiedler,[21] F. Filthaut,[29,30] W. Fisher,[57] H. E. Fisk,[45] M. Fortner,[47] H. Fox,[39] J. Franc,[7] S. Fuess,[45] P. H. Garbincius,[45] A. Garcia-Bellido,[63] J. A. García-González,[28] V. Gavrilov,[32] W. Geng,[12,57] C. E. Gerber,[46] Y. Gershtein,[60] G. Ginther,[45,63] O. Gogota,[38] G. Golovanov,[31] P. D. Grannis,[64] S. Greder,[16] H. Greenlee,[45] G. Grenier,[17] Ph. Gris,[10] J.-F. Grivaz,[13] A. Grohsjean,[15,c] S. Grünendahl,[45] M. W. Grünewald,[26] T. Guillemin,[13] G. Gutierrez,[45] P. Gutierrez,[67] J. Haley,[68] L. Han,[4] K. Harder,[41] A. Harel,[63] J. M. Hauptman,[52] J. Hays,[40] T. Head,[41] T. Hebbeker,[18] D. Hedin,[47] H. Hegab,[68] A. P. Heinson,[43] U. Heintz,[69] C. Hensel,[1] I. Heredia-De La Cruz,[28,d] K. Herner,[45] G. Hesketh,[41,f] M. D. Hildreth,[51] R. Hirosky,[73] T. Hoang,[44] J. D. Hobbs,[64] B. Hoeneisen,[9] J. Hogan,[72] M. Hohlfeld,[21] J. L. Holzbauer,[58] I. Howley,[70] Z. Hubacek,[7,15] V. Hynek,[7] I. Iashvili,[62] Y. Ilchenko,[71] R. Illingworth,[45] A. S. Ito,[45] S. Jabeen,[45,m] M. Jaffré,[13] A. Jayasinghe,[67] M. S. Jeong,[27] R. Jesik,[40] P. Jiang,[4] K. Johns,[42] E. Johnson,[57] M. Johnson,[45] A. Jonckheere,[45] P. Jonsson,[40] J. Joshi,[43] A. W. Jung,[45,o] A. Juste,[36] E. Kajfasz,[12] D. Karmanov,[33] I. Katsanos,[59] M. Kaur,[23] R. Kehoe,[71] S. Kermiche,[12] N. Khalatyan,[45] A. Khanov,[68] A. Kharchilava,[62] Y. N. Kharzheev,[31] I. Kiselevich,[32] J. M. Kohli,[23] A. V. Kozelov,[34] J. Kraus,[58] A. Kumar,[62] A. Kupco,[8] T. Kurča,[17] V. A. Kuzmin,[33] S. Lammers,[49] P. Lebrun,[17] H. S. Lee,[27] S. W. Lee,[52] W. M. Lee,[45] X. Lei,[42] J. Lellouch,[14] D. Li,[14] H. Li,[73] L. Li,[43] Q. Z. Li,[45] J. K. Lim,[27] D. Lincoln,[45] J. Linnemann,[57] V. V. Lipaev,[34] R. Lipton,[45] H. Liu,[71] Y. Liu,[4] A. Lobodenko,[35] M. Lokajicek,[8] R. Lopes de Sa,[45] R. Luna-Garcia,[28,g] A. L. Lyon,[45] A. K. A. Maciel,[1] R. Madar,[19] R. Magaña-Villalba,[28] S. Malik,[59] V. L. Malyshev,[31] J. Mansour,[20] J. Martínez-Ortega,[28] R. McCarthy,[64] C. L. McGivern,[41] M. M. Meijer,[29,30] A. Melnitchouk,[45] D. Menezes,[47] P. G. Mercadante,[3] M. Merkin,[33] A. Meyer,[18] J. Meyer,[20,I] F. Miconi,[16] N. K. Mondal,[25] M. Mulhearn,[73] E. Nagy,[12] M. Narain,[69] R. Nayyar,[42] H. A. Neal,[56] J. P. Negret,[5] P. Neustroev,[35] H. T. Nguyen,[73] T. Nunnemann,[22] J. Orduna,[72] N. Osman,[12] J. Osta,[51] A. Pal,[70] N. Parashar,[50] V. Parihar,[69] S. K. Park,[27] R. Partridge,[69,e] N. Parua,[49] A. Patwa,[65,j] B. Penning,[40] M. Perfilov,[33] Y. Peters,[41] K. Petridis,[41] G. Petrillo,[63] P. Pétroff,[13] M. -A. Pleier,[65] V. M. Podstavkov,[45] A. V. Popov,[34] M. Prewitt,[72] D. Price,[41] N. Prokopenko,[34] J. Qian,[56] A. Quadt,[20] B. Quinn,[58] P. N. Ratoff,[39] I. Razumov,[34] I. Ripp-Baudot,[16] F. Rizatdinova,[68] M. Rominsky,[45] A. Ross,[39] C. Royon,[15] P. Rubinov,[45] R. Ruchti,[51] G. Sajot,[11] A. Sánchez-Hernández,[28] M. P. Sanders,[22] A. S. Santos,[1,h] G. Savage,[45] M. Savitskyi,[38] L. Sawyer,[54] T. Scanlon,[40] R. D. Schamberger,[64] Y. Scheglov,[35] H. Schellman,[48] M. Schott,[21] C. Schwanenberger,[41] R. Schwienhorst,[57] J. Sekaric,[53] H. Severini,[67] E. Shabalina,[20] V. Shary,[15] S. Shaw,[41] A. A. Shchukin,[34] V. Simak,[7] P. Skubic,[67] P. Slattery,[63] D. Smirnov,[51] G. R. Snow,[59] J. Snow,[66] S. Snyder,[65] S. Söldner-Rembold,[41] L. Sonnenschein,[18] K. Soustruznik,[6] J. Stark,[11] D. A. Stoyanova,[34] M. Strauss,[67] L. Suter,[41] P. Svoisky,[67] M. Titov,[15] V. V. Tokmenin,[31] Y.-T. Tsai,[63] D. Tsybychev,[64] B. Tuchming,[15] C. Tully,[61] L. Uvarov,[35] S. Uvarov,[35] S. Uzunyan,[47] R. Van Kooten,[49] W. M. van Leeuwen,[29] N. Varelas,[46] E. W. Varnes,[42] I. A. Vasilyev,[34] A. Y. Verkheev,[31] L. S. Vertogradov,[31] M. Verzocchi,[45] M. Vesterinen,[41] D. Vilanova,[15] P. Vokac,[7] H. D. Wahl,[44] M. H. L. S. Wang,[45] J. Warchol,[51] G. Watts,[74] M. Wayne,[51] J. Weichert,[21] L. Welty-Rieger,[48] M. R. J. Williams,[49,n] G. W. Wilson,[53] M. Wobisch,[54] D. R. Wood,[55] T. R. Wyatt,[41] Y. Xie,[45] R. Yamada,[45] S. Yang,[4] T. Yasuda,[45] Y. A. Yatsunenko,[31] W. Ye,[64] Z. Ye,[45] H. Yin,[45] K. Yip,[65] S. W. Youn,[45] J. M. Yu,[56] J. Zennamo,[62] T. G. Zhao,[41] B. Zhou,[56] J. Zhu,[56] M. Zielinski,[63] D. Zieminska,[49] and L. Zivkovic[14]

(The D0 Collaboration)

[1]*LAFEX, Centro Brasileiro de Pesquisas Físicas, Rio de Janeiro, Brazil*
[2]*Universidade do Estado do Rio de Janeiro, Rio de Janeiro, Brazil*
[3]*Universidade Federal do ABC, Santo André, Brazil*
[4]*University of Science and Technology of China, Hefei, People's Republic of China*

2470-0010/2016/94(9)/092004(21)

[5]*Universidad de los Andes, Bogotá, Colombia*
[6]*Charles University, Faculty of Mathematics and Physics, Center for Particle Physics, Prague, Czech Republic*
[7]*Czech Technical University in Prague, Prague, Czech Republic*
[8]*Institute of Physics, Academy of Sciences of the Czech Republic, Prague, Czech Republic*
[9]*Universidad San Francisco de Quito, Quito, Ecuador*
[10]*LPC, Université Blaise Pascal, CNRS/IN2P3, Clermont, France*
[11]*LPSC, Université Joseph Fourier Grenoble 1, CNRS/IN2P3, Institut National Polytechnique de Grenoble, Grenoble, France*
[12]*CPPM, Aix-Marseille Université, CNRS/IN2P3, Marseille, France*
[13]*LAL, Université Paris-Sud, CNRS/IN2P3, Orsay, France*
[14]*LPNHE, Universités Paris VI and VII, CNRS/IN2P3, Paris, France*
[15]*CEA, Irfu, SPP, Saclay, France*
[16]*IPHC, Université de Strasbourg, CNRS/IN2P3, Strasbourg, France*
[17]*IPNL, Université Lyon 1, CNRS/IN2P3, Villeurbanne, France and Université de Lyon, Lyon, France*
[18]*III. Physikalisches Institut A, RWTH Aachen University, Aachen, Germany*
[19]*Physikalisches Institut, Universität Freiburg, Freiburg, Germany*
[20]*II. Physikalisches Institut, Georg-August-Universität Göttingen, Göttingen, Germany*
[21]*Institut für Physik, Universität Mainz, Mainz, Germany*
[22]*Ludwig-Maximilians-Universität München, München, Germany*
[23]*Panjab University, Chandigarh, India*
[24]*Delhi University, Delhi, India*
[25]*Tata Institute of Fundamental Research, Mumbai, India*
[26]*University College Dublin, Dublin, Ireland*
[27]*Korea Detector Laboratory, Korea University, Seoul, Korea*
[28]*CINVESTAV, Mexico City, Mexico*
[29]*Nikhef, Science Park, Amsterdam, the Netherlands*
[30]*Radboud University Nijmegen, Nijmegen, the Netherlands*
[31]*Joint Institute for Nuclear Research, Dubna, Russia*
[32]*Institute for Theoretical and Experimental Physics, Moscow, Russia*
[33]*Moscow State University, Moscow, Russia*
[34]*Institute for High Energy Physics, Protvino, Russia*
[35]*Petersburg Nuclear Physics Institute, St. Petersburg, Russia*
[36]*Institució Catalana de Recerca i Estudis Avançats (ICREA) and Institut de Física d'Altes Energies (IFAE), Barcelona, Spain*
[37]*Uppsala University, Uppsala, Sweden*
[38]*Taras Shevchenko National University of Kyiv, Kiev, Ukraine*
[39]*Lancaster University, Lancaster LA1 4YB, United Kingdom*
[40]*Imperial College London, London SW7 2AZ, United Kingdom*
[41]*The University of Manchester, Manchester M13 9PL, United Kingdom*
[42]*University of Arizona, Tucson, Arizona 85721, USA*
[43]*University of California Riverside, Riverside, California 92521, USA*
[44]*Florida State University, Tallahassee, Florida 32306, USA*
[45]*Fermi National Accelerator Laboratory, Batavia, Illinois 60510, USA*
[46]*University of Illinois at Chicago, Chicago, Illinois 60607, USA*
[47]*Northern Illinois University, DeKalb, Illinois 60115, USA*
[48]*Northwestern University, Evanston, Illinois 60208, USA*
[49]*Indiana University, Bloomington, Indiana 47405, USA*
[50]*Purdue University Calumet, Hammond, Indiana 46323, USA*
[51]*University of Notre Dame, Notre Dame, Indiana 46556, USA*
[52]*Iowa State University, Ames, Iowa 50011, USA*
[53]*University of Kansas, Lawrence, Kansas 66045, USA*
[54]*Louisiana Tech University, Ruston, Louisiana 71272, USA*
[55]*Northeastern University, Boston, Massachusetts 02115, USA*
[56]*University of Michigan, Ann Arbor, Michigan 48109, USA*
[57]*Michigan State University, East Lansing, Michigan 48824, USA*
[58]*University of Mississippi, University, Mississippi 38677, USA*
[59]*University of Nebraska, Lincoln, Nebraska 68588, USA*
[60]*Rutgers University, Piscataway, New Jersey 08855, USA*
[61]*Princeton University, Princeton, New Jersey 08544, USA*

[62]*State University of New York, Buffalo, New York 14260, USA*
[63]*University of Rochester, Rochester, New York 14627, USA*
[64]*State University of New York, Stony Brook, New York 11794, USA*
[65]*Brookhaven National Laboratory, Upton, New York 11973, USA*
[66]*Langston University, Langston, Oklahoma 73050, USA*
[67]*University of Oklahoma, Norman, Oklahoma 73019, USA*
[68]*Oklahoma State University, Stillwater, Oklahoma 74078, USA*
[69]*Brown University, Providence, Rhode Island 02912, USA*
[70]*University of Texas, Arlington, Texas 76019, USA*
[71]*Southern Methodist University, Dallas, Texas 75275, USA*
[72]*Rice University, Houston, Texas 77005, USA*
[73]*University of Virginia, Charlottesville, Virginia 22904, USA*
[74]*University of Washington, Seattle, Washington 98195, USA*

(Received 23 May 2016; published 23 November 2016)

The inclusive cross section of top quark-antiquark pairs produced in $p\overline{p}$ collisions at $\sqrt{s} = 1.96$ TeV is measured in the lepton + jets and dilepton decay channels. The data sample corresponds to 9.7 fb^{-1} of integrated luminosity recorded with the D0 detector during Run II of the Fermilab Tevatron Collider. Employing multivariate analysis techniques we measure the cross section in the two decay channels and we perform a combined cross section measurement. For a top quark mass of 172.5 GeV, we measure a combined inclusive top quark-antiquark pair production cross section of $\sigma_{t\bar{t}} = 7.26 \pm 0.13(\mathrm{stat})^{+0.57}_{-0.50}(\mathrm{syst})$ pb which is consistent with standard model predictions. We also perform a likelihood fit to the measured and predicted top quark mass dependence of the inclusive cross section, which yields a measurement of the pole mass of the top quark. The extracted value is $m_t = 172.8 \pm 1.1(\mathrm{theo})^{+3.3}_{-3.1}(\mathrm{exp})$ GeV.

DOI: 10.1103/PhysRevD.94.092004

I. INTRODUCTION

The top quark, discovered by the CDF and D0 experiments in 1995 [1,2], is the heaviest of all elementary particles in the standard model (SM). The production of top quark-antiquark pairs ($t\bar{t}$) at the Fermilab Tevatron Collider is dominated by the quark-antiquark ($q\overline{q}$) annihilation process. The measurement of the inclusive $t\bar{t}$ production cross section provides a direct test of quantum chromodynamics (QCD), the theory of the strong interaction. Inclusive $t\bar{t}$ production cross sections have been previously measured at the Tevatron [3,4] and the LHC [5–7]. In this article we present a measurement using a refined analysis technique, which is optimized to be less dependent on the top quark mass. Compared to the previous D0 result [3] we employ nearly a factor of 2 more data, which allows for higher precision tests of perturbative QCD (pQCD).

The mass of the top quark has been directly measured with a precision of less than 0.43% in a single measurement [8]. The Tevatron combination currently yields a top quark mass of 174.34 ± 0.64 GeV [9]. The direct measurements employed for the Tevatron combination are based on analysis techniques which use $t\bar{t}$ events provided by Monte Carlo (MC) simulation for different assumed values of the top quark mass m_t. Applying these techniques to data yields a mass quantity corresponding to the top quark mass scheme implemented in the MC and we refer to that quantity as the “MC mass” or m_t^{MC}. Theoretical arguments

---

[a] Visitor from Augustana College, Sioux Falls, South Dakota, USA.
[b] Visitor from The University of Liverpool, Liverpool, United Kingdom.
[c] Visitor from DESY, Hamburg, Germany.
[d] Visitor from CONACyT, Mexico City, Mexico.
[e] Visitor from SLAC, Menlo Park, California, USA.
[f] Visitor from University College London, London, United Kingdom.
[g] Visitor from Centro de Investigacion en Computacion—IPN, Mexico City, Mexico.
[h] Visitor from Universidade Estadual Paulista, São Paulo, Brazil.
[i] Visitor from Karlsruher Institut für Technologie (KIT)—Steinbuch Centre for Computing (SCC), D-76128 Karlsruhe, Germany.
[j] Visitor from Office of Science, U.S. Department of Energy, Washington, D.C. 20585, USA.
[k] Visitor from American Association for the Advancement of Science, Washington, D.C. 20005, USA.
[l] Visitor from Kiev Institute for Nuclear Research, Kiev, Ukraine.
[m] Visitor from University of Maryland, College Park, Maryland 20742, USA.
[n] Visitor from European Orgnaization for Nuclear Research (CERN), Geneva, Switzerland.
[o] Visitor from Purdue University, West Lafayette, Indiana 47907, USA.

suggest that m_t^{MC} is within about 1 GeV of the well-defined top quark pole mass [10]. An alternative measurement approach employs the inclusive $t\bar{t}$ cross section to extract the mass of the top quark m_t. We assume the SM cross section dependence on m_t as provided by the highest order of pQCD available at this time, namely a next-to-next-to-leading-order (NNLO) calculation. Comparing the dependence of the inclusive cross section on m_t, as calculated in pQCD, with the experimental measurement, accounting for the variation of the acceptance with m_t, yields a theoretically well-defined top quark pole mass. We employ this approach to extract a top quark pole mass with reduced experimental uncertainties due to our optimized analysis technique.

Events are selected in the lepton + jets (ℓ + jets) and dilepton ($\ell\ell$) top quark decay channels, where the lepton (ℓ) refers to either an electron or a muon. These channels correspond to $t\bar{t} \to W^+ bW^- \bar{b}$ decays, where in the ℓ + jets channel one of the two W bosons decays leptonically ($W \to \ell\nu$), while the other W boson decays hadronically ($W \to q\bar{q}'$). In the dilepton decay channel both W bosons decay leptonically. Both decay channels include small contributions from electrons and muons stemming from the decay of τ leptons ($t \to Wb \to \tau\nu_\tau b \to \ell\nu_\ell\nu_\tau b$).

II. MEASUREMENT STRATEGY AND OUTLINE

This measurement uses various multivariate analysis (MVA) techniques [11–13], as implemented in TMVA [14], to measure the inclusive cross section in the ℓ + jets and $\ell\ell$ decay channels. For the dilepton decay channel we use a discriminant solely based on the output distribution of the MVA employed to identify jets that are likely to originate from b quarks (b-tagged jets) [15]. This method is superior to a simple cut-and-count analysis since each $t\bar{t}$ event contains two b-quarks from the decays of top quarks. We refer to this method in the following as “b-ID MVA.” We construct a combined discriminant for events in the ℓ + jets decay channel to make the best use of the distinct topological signature of top quark events along with b-tagging information. We refer to this method in the following as “combined MVA.” We use the entire distribution of the MVA discriminants in each decay channel to build MC templates. We use nuisance parameters to profile systematic uncertainties and to constrain their impact using data. For a combined inclusive $t\bar{t}$ cross section measurement we simultaneously employ the discriminant distribution of the b-ID MVA in the dilepton decay channel and the combined MVA in the ℓ + jets decay channel in a nuisance-parameter-based profiling method. This combination benefits from the cross-calibration of the two different decay channels, leading to reduced systematic uncertainties.

This article is organized as follows. In Sec. III we provide a brief review of the relevant aspects of the D0 detector and object reconstruction. A brief description of our event simulation approach, the QCD predictions employed, and a discussion of the assumptions for the modeling of the signal and background contributions follows in Sec. IV. The selection requirements for $t\bar{t}$ events in the ℓ + jets and $\ell\ell$ decay channels are discussed in Sec. V. The determination of the sample composition in the two decay channels, the resulting event yields, and distributions of the data compared to MC are discussed in Sec. VI. The details of the MVA techniques employed in this measurement are described in Sec. VII. The methodology of the inclusive $t\bar{t}$ production cross section measurement is described in Sec. VIII, and the systematic uncertainties relevant for this measurement are discussed in Sec. IX. The results of the cross section measurement are presented in Sec. X, followed by the extraction of the top quark pole mass given in Sec. XI, and we conclude in Sec. XII.

III. THE D0 DETECTOR AND OBJECT RECONSTRUCTION

The D0 detector [16] consists of several subdetectors designed for identification and reconstruction of the products of $p\bar{p}$ collisions. A silicon microstrip tracker (SMT) [17,18] and central fiber tracker surround the interaction region for pseudorapidities[1] $|\eta| < 3$ and $|\eta| < 2.5$, respectively. These elements of the central tracking system are located within a superconducting solenoidal magnet generating a 1.9 T field, providing measurements for reconstructing event vertices and trajectories of charged particles. The SMT allows for a precision of 40 μm or better for the reconstructed primary $p\bar{p}$ interaction vertex (PV) in the plane transverse to the beam direction. The impact parameter of typical charged-particle trajectories relative to the PV is determined with a precision between 20 and 50 μm depending on the number of SMT hits and particle momentum. The impact parameter and its measurement uncertainty are key components of the lifetime-based identification of jets containing b quarks. Particle energies are measured using a liquid argon sampling calorimeter that is segmented into a central calorimeter covering $|\eta| < 1.1$, and two end calorimeters extending the coverage to $|\eta| = 4.2$. Outside of the calorimetry, trajectories of muons are measured using three layers of tracking detectors and scintillation trigger counters, and an iron toroidal magnet generating a 1.8 T field between the first two layers [19]. Plastic scintillator arrays are located in front of the end calorimeter cryostats to measure the luminosity [20,21]. The trigger and data acquisition systems are designed to accommodate the high luminosities provided by the Tevatron [22].

---

[1] The pseudorapidity $\eta = -\ln[\tan(\theta/2)]$ is measured relative to the center of the detector, and θ is the polar angle with respect to the proton beam direction. The azimuthal angle ϕ is orthogonal to θ. The z axis is pointing along the proton beam direction.

A. Object reconstruction

The object reconstruction is based on events identified by the D0 trigger system in which we require at least one lepton or at least one lepton and a jet. Since electrons mostly deposit energy in the electromagnetic (EM) calorimeter, the reconstruction and identification (ID) of electrons [23] is based on clusters in the EM calorimeter with an associated track. Such a track, as reconstructed by the central tracking detector, is required to have a minimum transverse momentum, p_T, of 5 GeV that points to the EM cluster within a window of $\Delta\eta \times \Delta\phi = 0.05 \times 0.05$. We define an angular separation $\Delta R = \sqrt{(\Delta\eta)^2 + (\Delta\phi)^2}$ based on the distance $R = \sqrt{\eta^2 + \phi^2}$ in the η-ϕ plane. Electron candidates are required to be isolated by only accepting events with $\Delta R(e, \text{jet}) > 0.5$ (the definition and reconstruction of a jet is discussed below). Further selection requirements on these electron candidates are applied by means of a multivariate analysis of the calorimeter shower profiles and tracking information. MC efficiencies are adjusted to match data efficiencies measured in electron enriched data samples.

The identification of muons [24] begins with a candidate formed using information from the muon system. Such a candidate is required to have a track, as reconstructed by the central tracking devices, associated with it. This association employs a χ^2 measure to match muon tracks provided by the muon detector with a track from the central tracking detector, taking into account effects from multiple scattering and energy loss, as well as the inhomogeneous magnetic field. Isolation criteria are applied based on the information from the hadronic and electromagnetic calorimeters and the central tracking devices. MC efficiencies are adjusted to match data efficiencies measured in muon enriched data samples.

Jets are reconstructed from energy depositions in the calorimeter using a midpoint cone algorithm [25] employing a cone size of 0.5. Jets containing a muon within an angular separation of $\Delta R(\mu, \text{jet}) < 0.5$ are considered to originate from a semileptonic b-quark decay and are corrected for the momentum carried away by the muon and the neutrino. For this correction, it is assumed that the neutrino carries the same momentum as the muon.

The jet energy scale (JES) [26] corrects the measured energy of the jet to the energy of its constituent particles. The JES is derived using a quark-jet-dominated $\gamma + \text{jet}$ sample, and corrects data and MC for the difference in detector responses between jets and electromagnetic showers. An additional correction based on the single-particle response accounts for the different characteristics of quark and gluon jets. This correction implements a calibration of the simulated response to single particles inside a jet using data [26]. Jets in MC simulations have their transverse momenta smeared so that the simulated resolution matches that observed in data. Calibrations of the jet reconstruction and identification efficiency in MC simulations are determined using $Z/\gamma^* + \text{jets}$data events. Jets are required to contain at least two tracks (see Sec. V), and in MC simulations the corresponding efficiency is adjusted to match that derived in dijet data.

The presence of a neutrino in the final state of the top quark decay can be detected only from the energy imbalance in the transverse plane, denoted by $\not{E}_T$. This is reconstructed from the vector sum of the transverse energies of all calorimeter cells above a certain threshold. The vector opposite to this total visible momentum vector is denoted the raw missing energy vector. The fully corrected $\not{E}_T$ is obtained after correcting for the effects of JES, muon momenta, and muon minimally ionizing deposition in the calorimeter.

IV. MONTE CARLO SIMULATIONS AND QCD PREDICTIONS

We use MC simulations to simulate physics processes, to model the reconstruction of the observables, and to estimate systematic uncertainties associated with the measurements. Different MC event generators are used to implement hard scattering processes based on leading-order (LO) and next-to-leading-order (NLO) QCD calculations, and are complemented with parton shower evolution programs. To simulate detector effects, generated events are passed through a detailed simulation of the D0 detector based on GEANT [27]. To account for effects from detector noise and additional overlapping $p\bar{p}$ interactions, events are randomly recorded in $p\bar{p}$ collisions and overlaid on the fully simulated MC events with the same instantaneous luminosity distribution as for data.

The $t\bar{t}$ samples are generated with MC@NLO version 3.4 [28] or with ALPGEN version 2.11 [29], which both produce only on-shell top quarks. For events generated with MC@NLO, the parton showering is performed with HERWIG version 6.510 [30]. Events generated with ALPGEN employ parton showering as implemented by PYTHIA version 6.409 [31] or HERWIG. We use the ALPGEN + PYTHIA signal sample as our default to measure the $t\bar{t}$ cross section and the alternative MC@NLO + HERWIG, or ALPGEN + HERWIG, signal samples to estimate systematic uncertainties related to effects of NLO corrections or parton showering (see Sec. IX), respectively. Single top quark production $(q\bar{q}' \to t\bar{b}, q'g \to tq\bar{b})$ is modeled using COMPHEP [32,33]. For events generated with COMPHEP, parton showering is implemented by PYTHIA. The choice of the parton distribution functions (PDFs) made in generating MC events is CTEQ6L1 [34], with the exception of MC@NLO and COMPHEP (for the t-channel single top quark production), where CTEQ6M [35] PDFs are used. For all the MC simulations involving the generation of top quarks, a top quark mass of $m_t = 172.5$ GeV is used. The difference with the current Tevatron top quark mass combination of 174.34 GeV [9] has negligible impact on the analysis. For the $t\bar{t} \to \ell +$ jets ($\ell\ell$) decay channel the branching fraction B of 0.342 ± 0.004 (0.04 ± 0.001) [36] is used. These values include electrons and muons originating from the leptonic decay of τ leptons ($\tau \to \ell \nu_\ell \nu_\tau$).

Several QCD predictions for inclusive $t\bar{t}$ cross sections have been calculated at higher orders than those included in the MC generators: approximate NNLO [37], fully resummed NNLO [38], and an approximate next-to-NNLO [39]. The scale used to calculate the inclusive $t\bar{t}$ cross sections is set to m_t. For normalization of our MC events, we employ the approximate NNLO QCD calculation (using $m_t = 172.5$ GeV and the CTEQ6M PDF), which yields $7.48^{+0.48}_{-0.67}(\text{scale} + \text{pdf})$ pb. The result of this approximate NNLO calculation is close to the fully resummed NNLO QCD calculation (using $m_t = 172.5$ GeV), which finds $\sigma^{\text{res}}_{\text{tot}} = 7.35^{+0.23}_{-0.27}(\text{scale}+\text{pdf})$ pb. The result of an approximate next-to-NNLO order calculation for $m_t = 173$ GeV finds $\sigma^{\text{res}}_{\text{tot}} = 7.37 \pm 0.39(\text{scale}+\text{pdf})$ pb, very close to the fully resummed NNLO calculation. Both use the MSTW2008 NNLO PDF [40].

We use the fully resummed NNLO QCD calculation as implemented in TOP++ [41] to derive the theoretical $t\bar{t}$ cross section dependence as a function of the top quark mass (see Sec. XI). The theoretical calculations use $\sqrt{s} = 1.96$ TeV as input parameter which is known at the Tevatron to a precision of 0.1%. This beam energy uncertainty yields a negligible 0.3% effect on the fully resummed NNLO $t\bar{t}$ cross section value.

A. Modeling of background contributions in the $\ell +$ jets decay channel

The main background to $t\bar{t}$ production in the $\ell +$ jets decay channel is the production of $W +$ jets, including jets originating from heavy quarks. These events are generated with ALPGEN interfaced to PYTHIA for showering and hadronization. The $W +$ jets final state can be split into four subsamples according to parton flavor: $Wb\bar{b} +$ jets, $Wc\bar{c} +$ jets, $Wc +$ jets, and W light partons + jets ($Wlp +$ jets), where light refers to gluons, u, d or s quarks. The additional "jets" in these $W +$ jets final states originate dominantly from gluon radiation. The $W +$ jets contribution dominates especially at the lower jet multiplicities. The LO ALPGEN cross sections are corrected for NLO effects as provided by MCFM [42]: the $W +$ jets cross section is multiplied by 1.30, and the cross sections of $W+$ heavy flavor (WHF) processes are additionally multiplied by a scale factor s^{WHF} of 1.47 for $Wb\bar{b} +$ jets and $Wc\bar{c} +$ jets and 1.27 for $Wc +$ jets. Apart from these theoretical corrections we constrain the absolute background normalization by employing the data as described below in Sec. VI. The p_T distribution of the W boson in MC simulation is reweighted to match the p_T distribution of Z bosons measured in D0 data [43] multiplied by the SM ratio of these two distributions calculated at NLO using RESBOS [44].

The second most dominant background contribution is due to multijet processes where a jet is misidentified as an electron in the $e +$ jets channel, or where a muon originating from the semileptonic decay of a heavy hadron appears to be isolated in the $\mu +$ jets channel. More details and a brief discussion on the determination of the multijet background are given in Sec. VI.

Other backgrounds include events from $Z/\gamma^* +$ jets production, which includes Z bosons and virtual photons (γ^*) decaying to electron, muon, or tau pairs. These events are generated with ALPGEN interfaced to PYTHIA for showering and hadronization. The LO ALPGEN predictions are corrected using the NLO calculation of MCFM. The $Z/\gamma^* +$ jets cross section is multiplied by 1.30. The heavy flavor components of the $Z/\gamma^* +$ jets cross sections, $Z/\gamma^* c\bar{c} +$ jets, $Z/\gamma^* b\bar{b} +$ jets, are multiplied by an additional 1.67 and 1.52, respectively. The simulated p_T distribution of the Z boson is reweighted to match the measured p_T distribution in $Z \to \ell\ell$ data [43].

The single top quark background originates from s- and t-channel production, which are normalized to the NLO cross sections of 1.04 and 2.26 pb [45], respectively. As the single top quark background yields only a few events passing all selection criteria described later, we do not consider the dependence of this background on m_t.

Diboson production (WW, WZ, and ZZ bosons) processes are another source of background and normalized to their NLO cross sections, calculated with MCFM, of 11.62 pb, 3.25 pb, and 1.33 pb, respectively.

B. Modeling of background contributions in the $\ell\ell$ decay channel

The backgrounds in the dilepton decay channel are smaller than in the $\ell +$ jets decay channel. The dominant source is $Z/\gamma^* +$ jets production, followed by diboson production. For both processes the modeling employs the same implementation as described above for the $\ell +$ jets decay channel.

The third most dominant source of background is multijet events, with the determination summarized in Sec. VI.

V. EVENT SELECTION

This analysis is based upon the full Tevatron data sample recorded by the D0 detector at $\sqrt{s} = 1.96$ TeV and, after applying data quality requirements, corresponding to an integrated luminosity of 9.7 fb^{-1} [21]. The general selection criteria applied to both the $\ell +$ jets and dilepton decay channels are summarized in the following:

(1) Accepted events have a PV within $|z_{\mathrm{PV}}| < 60$ cm of the center of the detector along the beam axis.
(2) The number of tracks associated with the PV is greater or equal three.
(3) After correcting the jet energy to the particle level, only jets with a transverse momentum $p_T > 20$ GeV and $|\eta| < 2.5$ are selected.
(4) Jets which satisfy the b-tagging requirement are required to have at least two tracks coming from the PV. More details on jet requirements for the individual decay channels are provided below.
(5) Identified leptons are required to originate from the PV by demanding $|\Delta z(\ell, \mathrm{PV})| < 1$ cm. These z values correspond to the point of closest approach to the beam line of these tracks.
(6) To ensure that electrons are isolated, an angular separation in ΔR of at least 0.5 between an electron and the closest jet is required.

The measurements in both decay channels employ the b-tagging discriminant output distribution as provided by the b-ID MVA. The discriminant combines variables that characterize the presence and properties of secondary vertices and tracks within jets [15]. We do not impose any requirements on this discriminant; instead we employ the entire distribution to measure the inclusive cross section as described in Sec. VII.

The specific selection requirements for $\ell +$ jets and $\ell\ell$ events are described below; the requirements are chosen such that the selections are mutually exclusive.

A. Event selection in the $\ell +$ jets decay channel

The selection requirements for the cross section measurement for the $\ell +$ jets channel are very similar to the ones described in Ref. [46] and are summarized briefly in the following:

(1) The trigger requirement is a logical “OR” of the conditions for at least “one lepton” and for at least “a lepton plus a jet” in an event. Lepton trigger thresholds of 15 or 10 GeV were implemented for the single lepton trigger or the lepton plus jet trigger, respectively.
(2) Exactly one isolated lepton with a transverse momentum $p_T > 20$ GeV and $|\eta| < 1.1$ (for electrons) or $|\eta| < 2$ (for muons) is required. Events with more than one lepton satisfying these criteria are rejected.
(3) We require $\not{E}_T > 20$ GeV.
(4) For the $\mu +$ jets sample we remove misreconstructed muons by requiring upper limits on the transverse mass of the muon $+ \not{E}_T$ system, M_T^W, of $M_T^W < 250$ GeV and $\not{E}_T < 250$ GeV. To further remove such events, we employ an additional requirement on the significance of the track curvature described in more detail in Ref. [46].
(5) To reduce multijet background we require a minimum separation between the direction of the lepton and the direction of the missing momentum [46]: $\Delta\phi(e,\not{E}_T) > 2.2 - 0.045 \cdot \not{E}_T/\mathrm{GeV}$ and $\Delta\phi(\mu,\not{E}_T) > 2.1 - 0.035 \cdot \not{E}_T/\mathrm{GeV}$.
(6) At least two jets are required. To suppress jets from additional collisions, jets are required to contain at least two tracks with a closest approach in z to the PV of less than 1 cm.

B. Event selection in the dilepton decay channel

In addition to the general selection requirements discussed in the opening of this section, additional requirements specific to the dilepton channel are made. The selection requirements for this cross section measurement are very similar to those used for the leptonic asymmetry measurements in the dilepton channel published earlier [47] and are summarized briefly in the following list.

(1) In the $e\mu$ channel, no explicit trigger requirement is applied, whereas in the ee or $\mu\mu$ channels single lepton triggers with thresholds at 15 GeV are employed.
(2) Electrons are required to have a transverse momentum of $p_T > 15$ GeV and $|\eta| < 2.5$. We exclude the $1.1 < |\eta| < 1.5$ region with poor resolution.
(3) Muons are selected with $p_T > 15$ GeV and $|\eta| < 2$. To remove misreconstructed muons we require muons to have $p_T < 200$ GeV for the dimuon channel.
(4) For the $e\mu$ channel exactly one electron and one or more muons are required.
(5) For the $\mu\mu$ channel two or more muons are required.
(6) For the ee channel two or more electrons are required.
(7) The two selected leptons must have opposite charges. If more than one oppositely charged lepton pair is found, the lepton pair with the largest p_T scalar sum is chosen.
(8) At least one jet is required in the $e\mu$ channel and at least two jets are required in the $\mu\mu$ and ee channel.
(9) Additional quality requirements are imposed to remove background from bremsstrahlung.
(10) We further reduce background contributions by imposing the following topological requirements: in the ee channel we require a $\not{E}_T$ significance of ≥ 5, in the $\mu\mu$ channel we require $\not{E}_T > 40$ GeV and a $\not{E}_T$ significance of ≥ 2.5, and in the $e\mu$ channel we require $H_T > 110$ GeV, where $H_T = p_T(\text{leading lepton}) + p_T(2\,\text{leading jets})$. More details are described in Ref. [47].

VI. SAMPLE COMPOSITIONS

We distinguish between instrumental backgrounds and irreducible backgrounds from processes with final states identical to $t\bar{t}$. Instrumental backgrounds are due to multijet processes where one or more jets are misidentified as an electron, or where one or more muons originating from the semileptonic decay of a heavy hadron appear to be isolated, and hence fulfill all selection requirements of a lepton stemming from the decay of a top quark. Irreducible backgrounds are for example due to $W+\text{jets}$ or $Z/\gamma^* + \text{jets}$ processes with the same final state as the $\ell + \text{jets}$ and $\ell\ell$ top quark decay channel. Systematic uncertainties on the determination of the sample composition are discussed in Sec. IX A 4. The following section describes the composition of the input or "pre-fit" $\ell + \text{jets}$ and $\ell\ell$ samples, which are used to extract the $t\bar{t}$ cross section as described in Sec. VIII.

A. Determination of the $\ell + \text{jets}$ sample composition

The irreducible background processes are estimated using MC simulations as described in Sec. IV. Compared to the $\ell\ell$ channel, the $\ell + \text{jets}$ channel has a larger background fraction, each with larger systematic uncertainties than in the $\ell\ell$ channel. Since most of this background arises from $W + \geq 2$ jets production we estimate this contribution following the same approach as for the measurement of the differential $t\bar{t}$ cross section [46]. The $W + \text{jets}$ cross section is iteratively scaled for each jet multiplicity bin separately by a $W + \text{jets}$ heavy-flavor scale factor $s_{\text{fit}}^{\text{WHF}}$ and $W + \text{jets}$ light-flavor scale factor $s_{\text{fit}}^{\text{WLF}}$ to match the number of data events after subtraction of all other instrumental and irreducible background contributions as well as the signal contribution. This approach yields reasonable initial values for the log-likelihood profile fit (introduced in Sec. VIII). The details of the estimation of systematic uncertainties are described in Sec. IX A 4.

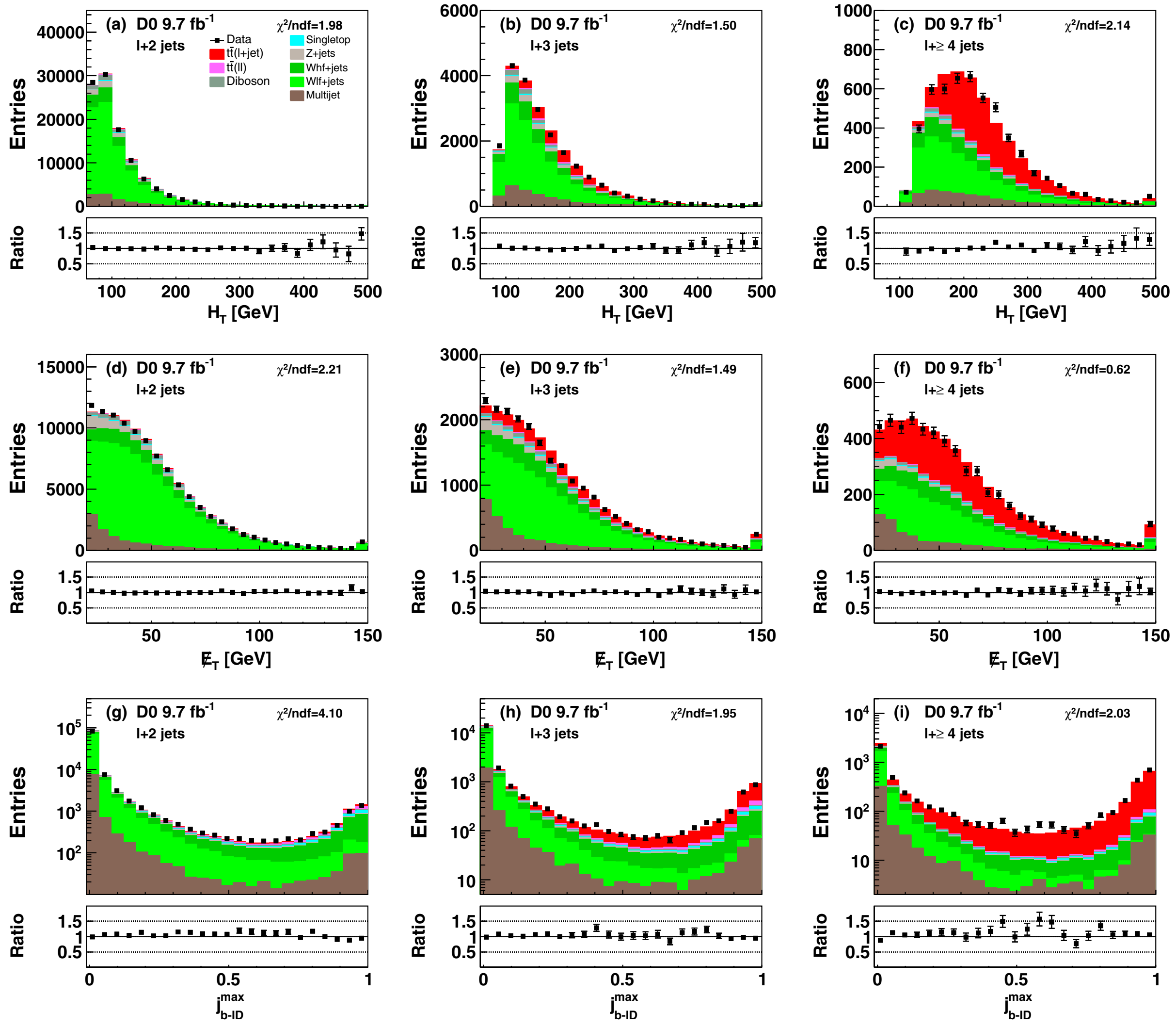

FIG. 1. Distributions of (a)–(c) the scalar sum of the p_T values of the lepton and jets, H_T, (d)–(f) $\not{E}_T$ and (g)–(i) the maximal MVA b-ID value of all jets, $j_{\text{b-ID}}^{\text{max}}$, for events with a lepton and two, three or four or more jets. The data are compared to the sum of predicted contributions from signal and background processes, using the theoretical value of the inclusive $t\bar{t}$ cross section of 7.48 pb [37] and $m_t = 172.5$ GeV. The highest bin in the histograms includes overflows. The ratios of data to the sum of the signal and all background contributions are shown in the panels below the individual distributions. Only statistical uncertainties of the data are shown and the χ^2/ndf values only take statistical uncertainties into account.

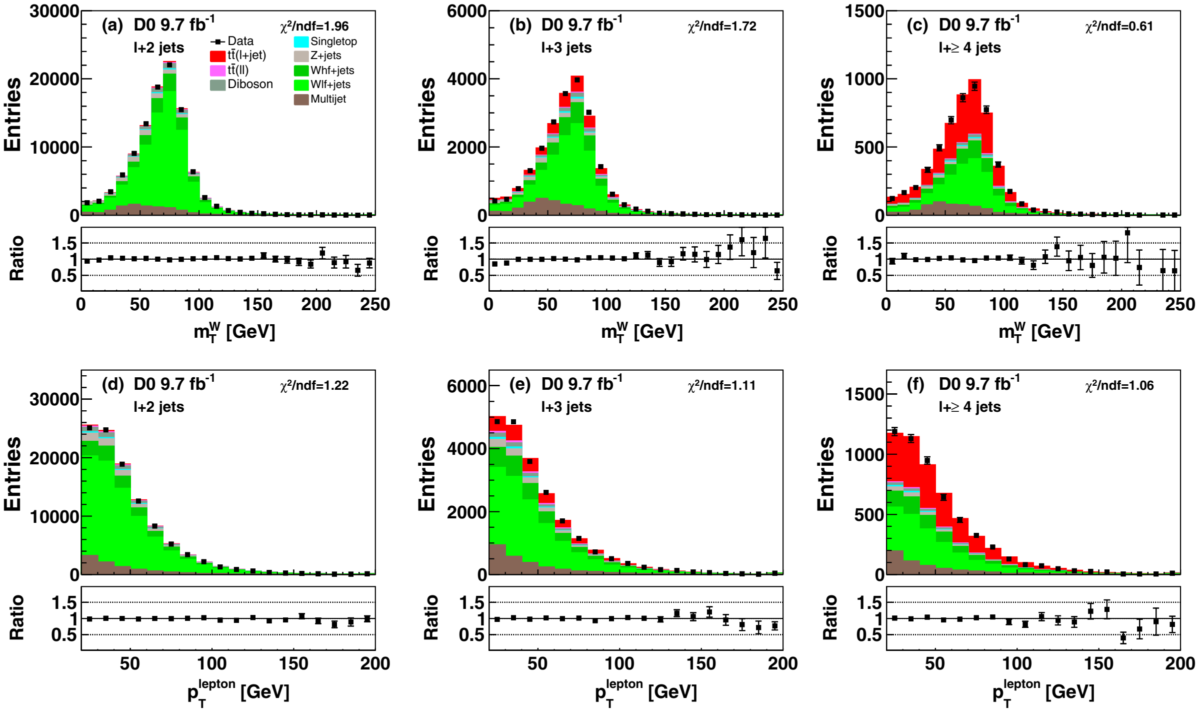

FIG. 2. Distributions of (a)–(c) the transverse mass of the lepton + $\not{E}_T$ system, m_T^W, and (d)–(f) p_T^{lepton} for events with a lepton and two, three or four or more jets. The data are compared to the sum of predicted contributions from signal and background processes, using the theoretical value of the inclusive $t\bar{t}$ cross section of 7.48 pb [37] and $m_t = 172.5$ GeV. The highest bin in the histograms includes overflows. The ratios of data to the sum of the signal and all background contributions are shown in the panels below the distributions. Only statistical uncertainties of the data are shown and the χ^2/ndf values only take statistical uncertainties into account.

Data-driven and MC methods are combined in the "matrix method" [3,48], which is employed to model the instrumental background originating from multijet (MJ) processes in the ℓ + jets channel. The MJ contribution is determined employing two samples of ℓ + jets events: one applying the nominal lepton selection requirements and one with looser lepton selection requirements denoted "loose." In addition, an orthogonal data sample is defined by requiring $\not{E}_T < 10$ GeV (the nominal requirement is $\not{E}_T > 20$ GeV) and the above selection criteria for the signal sample. This data sample is enriched in MJ events and any contributions from isolated leptons, as expected from MC, are subtracted from all considered distributions. No real isolated leptons are assumed to be included. We determine the shape and absolute

TABLE I. Expected number of events in the ℓ + jets channel with two, three or ≥ four jets. The sum of signal and background agrees well with the number of data events by construction; uncertainties are statistical and systematic added in quadrature (see Sec. IX A 4 for details). Events from $t\bar{t}$ dilepton decays are treated as background and denoted as "$t\bar{t}\ell\ell$."

	ℓ + jets decay channel					
Process	$e + 2$ jets	$e + 3$ jets	$e+ \geq 4$ jets	$\mu + 2$ jets	$\mu + 3$ jets	$\mu+ \geq 4$ jets
Multijet	9160 ± 2350	2266 ± 550	464 ± 120	1546 ± 630	418 ± 170	99 ± 40
Single top	471 ± 60	129 ± 20	27 ± 5	331 ± 40	92 ± 10	20 ± 3
Wlp + jets	$37937\pm^{1350}_{700}$	$5544\pm^{200}_{100}$	$850\pm^{30}_{20}$	$32701\pm^{1150}_{600}$	$5313\pm^{200}_{100}$	$835\pm^{30}_{15}$
$(Wc\bar{c} + Wb\bar{b})$ + jets	$6020\pm^{1000}_{1400}$	$1502\pm^{250}_{350}$	$329\pm^{60}_{80}$	$4998\pm^{850}_{1150}$	$1391\pm^{250}_{300}$	$315\pm^{50}_{70}$
$Z/\gamma^* lp$ + jets	2031 ± 400	390 ± 80	57 ± 10	2557 ± 500	422 ± 80	49 ± 10
$(Z/\gamma^* c\bar{c} + Z/\gamma^* b\bar{b})$ + jets	369 ± 70	114 ± 20	24 ± 5	485 ± 100	120 ± 20	21 ± 5
Diboson	1926 ± 140	338 ± 20	52 ± 5	1417 ± 100	249 ± 20	40 ± 5
$t\bar{t}$ $\ell\ell$	566 ± 30	182 ± 10	31 ± 5	345 ± 20	118 ± 10	22 ± 5
$\sum$ background	58479 ± 2900	10465 ± 650	1834 ± 140	44381 ± 1650	8123 ± 350	1402 ± 80
$t\bar{t}$ ℓ + jets	669 ± 30	1460 ± 70	1177 ± 60	393 ± 20	1002 ± 50	909 ± 50
$\sum$(signal + background)	59148 ± 2900	11925 ± 650	3011 ± 140	44773 ± 1650	9125 ± 350	2310 ± 80
Data	59122	11905	3007	44736	9098	2325

TABLE II. Expected number of events in the $ee+\geq 2$ jets, $\mu\mu+\geq 2$ jets, $e\mu+1$ jets and $e\mu+\geq 2$ jets channels due to each process; uncertainties are statistical and systematic added in quadrature (see Sec. IX A 4 for details).

	dilepton decay channel			
Process	$ee+\geq 2$ jets	$\mu\mu+\geq 2$ jets	$e\mu+1$ jets	$e\mu+\geq 2$ jets
Multijet	$5.7\pm^{0.9}_{0.9}$	$7.0\pm^{3.3}_{2.6}$	$28.3\pm^{6.6}_{6.6}$	$32.5\pm^{7.4}_{7.4}$
$Z/\gamma^* \to \ell\ell+$ jets	$66.6\pm^{17.9}_{17.2}$	$107.6\pm^{22.1}_{22.0}$	$74.6\pm^{15.8}_{15.8}$	$57.5\pm^{13.8}_{13.4}$
Diboson	$9.9\pm^{2.4}_{2.2}$	$12.6\pm^{2.8}_{3.0}$	$38.5\pm^{4.6}_{4.2}$	$14.7\pm^{3.7}_{3.5}$
$\sum$ background	82.2 ± 18	172.2 ± 22	141.4 ± 18	104.7 ± 15
$t\bar{t}$ $\ell\ell$	107.7 ± 15	101.5 ± 12	86.5 ± 11	313.7 ± 38
$\sum$(signal + background)	190 ± 23	229 ± 25	228 ± 21	418 ± 42
Data	215	242	236	465

contribution (misidentification rate) of multijet events for different jet multiplicities by comparing this data sample with the data sample containing loose leptons but the same $\not{E}_T$ requirement.

Figures 1 and 2 show the modeling of the selected events in the $\ell+$jets sample with the background and signal contributions. The expected composition of the sample after the final selection is given in Table I.

B. Determination of the $\ell\ell$ sample composition

The main backgrounds in the dilepton final state originate from $Z/\gamma^* \to \ell\ell$ instrumental backgrounds, and diboson production (WW, WZ, ZZ). The $Z/\gamma^* \to \ell\ell$ and diboson backgrounds are evaluated from MC as described in Sec. IV B. We use a mixture of MC and data-driven approaches for the instrumental background determination. Similarly to the $\ell+$jets channel, the normalization of events with jets misidentified as electrons is estimated directly from data using the matrix method separately for the ee and $e\mu$ channels [47]. The estimation of the instrumental background from events with jets producing muons is based on events with two leptons of the same charge in the $\mu\mu$ and $e\mu$ channels, where for the latter the contribution from misidentified electrons is

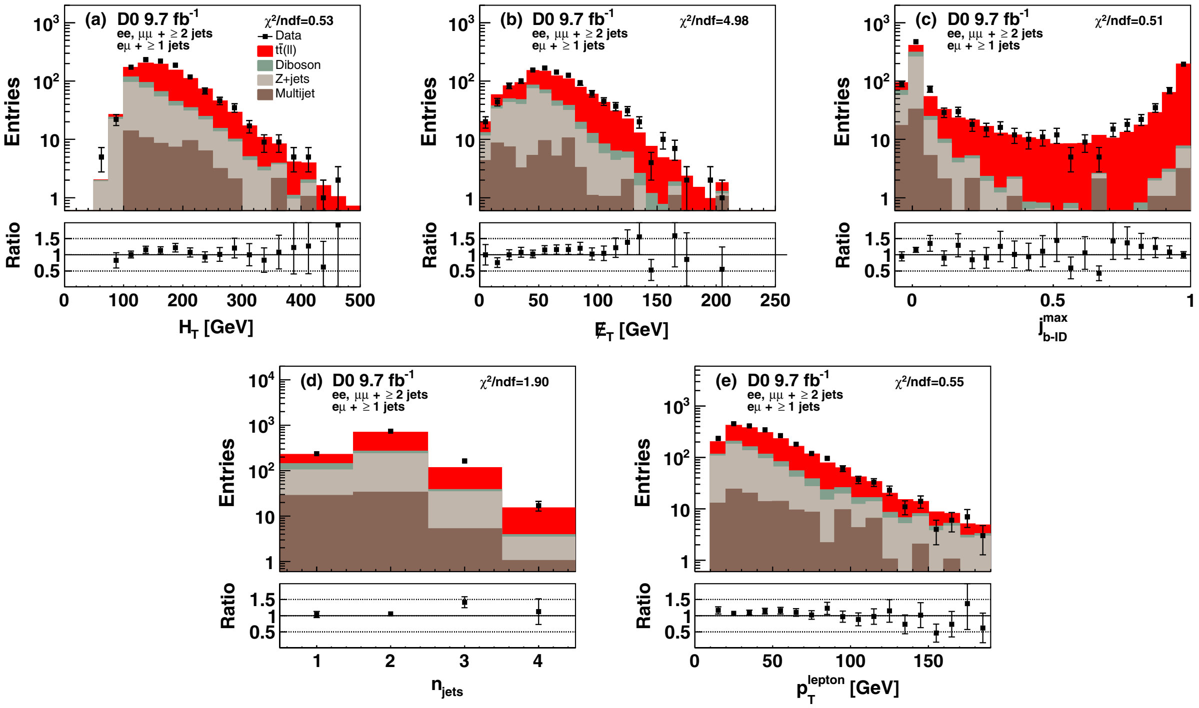

FIG. 3. Distributions of (a) the scalar sum, H_T, of the p_T values of the leading lepton and leading and second-leading jets, (b) $\not{E}_T$, (c) $j^{\max}_{\text{b-ID}}$, (d) the number of jets, and (e) lepton p_T for $\ell\ell$ final states with at least one jet in the $e\mu$ and at least two jets in the ee and $\mu\mu$ channels. The data are compared to the sum of predicted contributions from signal and background processes, using the theoretical value of 7.48 pb for the $t\bar{t}$ cross section and $m_t = 172.5$ GeV. The highest bin in the histograms includes overflows. The ratios of data to the sum of the signal and all background contributions are shown in the panels below the distributions. Only statistical uncertainties of the data are shown and the χ^2/ndf values only take statistical uncertainties into account.

subtracted beforehand. The electron misidentification rate for the matrix method is derived from an orthogonal data sample by requiring that the two leptons have the same charge. This sample is selected applying the same selection criteria as for $t\bar{t}$ events, but the final selection on H_T is replaced with requiring $\not{E}_T$ significance < 15 to avoid contribution from $W \to e\nu +$ jets events. The remaining contribution of the instrumental background is small, and we combine the MJ and $W +$ jets components to reduce the statistical uncertainty on the background estimate. The shape of the MJ template is derived using a looser electron selection of only $e\mu$ events and employed for all $\ell\ell$ channels. Since the MJ contribution in the ee and $\mu\mu$ sample is small the difference in shape is not significant.

The yields, after applying the described selection, are given in Table II for the individual channels.

Figure 3 demonstrates the quality of the modeling of the selected events in the $\ell\ell$ sample with the background and signal contributions, using a theoretical inclusive $t\bar{t}$ cross section of 7.48 pb [37] and $m_t = 172.5$ GeV. The slight disagreement in the $\not{E}_T$ distribution between data and the sum of signal and background contributions is covered by systematic uncertainties related to the JES and jet p_T resolution.

VII. MULTIVARIATE MEASUREMENT TECHNIQUES

The inclusive $t\bar{t}$ cross section $\sigma(t\bar{t})$ is measured using the different MVA techniques introduced in Sec. II. We use different discriminant output distributions of decision trees to separate the signal from the background for the $\ell +$ jets and $\ell\ell$ final states. To construct the MVA, the event sample is subsequently split into smaller samples until each event is placed in one of a set of distinct nodes. At each splitting point the separation is optimized by employing training samples for the signal and background contributions. The output or discriminant value provides the probability of an event to be signal. In the case of the combined MVA applied in the $\ell +$ jets channel we use each individual background contribution in the training process and verify that there is no bias due to overtraining of the method. We employ a method called "boosted decision trees with gradients" (BDTG) [49]. The BDTG implements additional weights to minimize classification errors in the training sample and improve signal to background separation. To measure the cross section we perform a log-likelihood profile fit of MC simulation templates to the data using a nuisance parameter for every source of systematic uncertainty as described in Sec. VIII.

A. MVA methods in the $\ell +$ jets channel

Events in the $\ell +$ jets channel are separated into six different samples according to the lepton type and the number of jets, $n_{\mathrm{jet}} = 2, 3, \geq 4$. We studied a further separation according to the number of b-tagged jets which gave increased systematic uncertainties and was not used for the final measurement. To build a discriminant, a total of 50 variables were analyzed. The individual distributions are verified to have a good modeling of the data by the MC by means of a Kolmogorov-Smirnov test [50] and a χ^2 test. We exclude all variables with poor modeling of the data. One variable among those studied, namely the maximal MVA b-ID value of all jets in the event, $j^{\max}_{\mathrm{b-ID}}$, shows only moderately good modeling of the data by MC [see Figs. 1(g)–1(i)]. However, the data are reasonably described when considering systematic uncertainties related to b-tagging. The $j^{\max}_{\mathrm{b-ID}}$ variable provides good separation power, and hence we use that variable in the discriminant.

Depending on the number of jets in an event, at least 24 variables are selected as input to the combined MVA for each jet multiplicity and lepton type bin (see the Appendix for a detailed variable description). In particular we include various MVA b-ID discriminants into the combined MVA discriminant, which allows superior signal-to-background separation, as discussed in the following paragraph. All selected variables are defined in the Appendix. Adding more variables has a negligible effect on the signal-to-background separation of the discriminant.

Figure 4 shows the separation of signal from background events in the $\ell +$ jets decay channel using as an example events with exactly three jets in the $e +$ jets channel. In this figure we show the performance of the combined MVA discriminant compared to the performance of a similar MVA discriminant that does not include the $j^{\max}_{\mathrm{b-ID}}$ input variable (combined MVA). For comparison we also show the performance of the MVA solely based on $j^{\max}_{\mathrm{b-ID}}$. The b-ID MVA has a higher signal and lower background

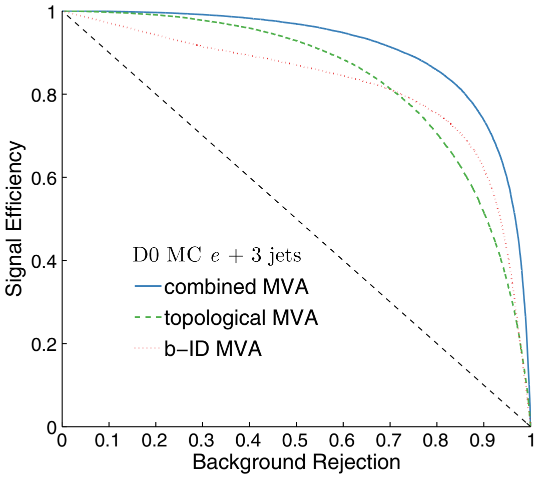

FIG. 4. Signal efficiency vs background rejection for different MVA choices for the $e + 3$ jets sample. For details, see text in Sec. VII. The dashed line from (0,1) to (1,0) is shown for reference.

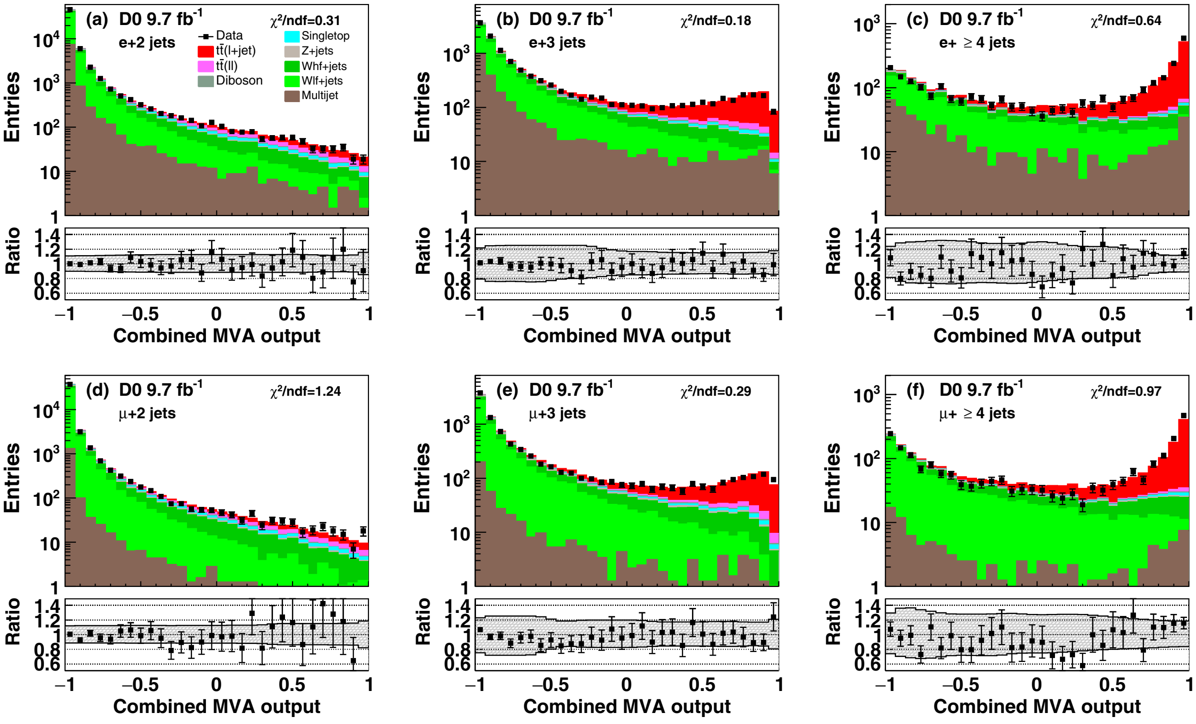

FIG. 5. Pre-fit output distributions of the combined MVA discriminant using the theoretical $t\bar{t}$ cross section and $m_t = 172.5$ GeV for the $e+$ two, three or four or more jets [panels (a)–(c)], and for the $\mu+$ two, three or four or more jets [panels (d)–(f)]. Statistical uncertainties of the data are shown and the pre-fit systematic uncertainties are indicated by the hashed band in the bottom panel of the histogram. The χ^2/ndf values take statistical and systematic uncertainties into account.

efficiency than the combined MVA for a signal efficiency less than about 80%. Above this point the combined MVA surpasses the b-ID MVA. Compared to these two MVA methods the combined MVA shows superior behavior, with the area under the curve increased by 6–10%.

Figure 5 shows the pre-fit MVA output distributions of the combined MVA method using a theoretical $t\bar{t}$ cross section of 7.48 pb.

B. MVA b-jet method in the $\ell\ell$ channel

We measure the $t\bar{t}$ production cross section in the $\ell\ell$ channel using $j^{\mathrm{max}}_{\mathrm{b-ID}}$ to separate signal from background. Events in the dilepton channel are separated into samples according to the lepton type and the number of jets. Due to the small background contribution and the size of the signal contribution in the dilepton channel, the separation provided by the $j^{\mathrm{max}}_{\mathrm{b-ID}}$ is sufficiently good and the combined MVA was not employed for the $\ell\ell$ channel.

The MVA output distributions in the dilepton channel allow one to distinguish between $t\bar{t}$ events dominantly located at high output values and the most dominant $Z/\gamma^* +$jets background contribution typically located at low output values. For the $e\mu$ channel we split the sample into subsamples with exactly one and ≥ two jets, whereas for ee and $\mu\mu$ only events with two or more jets are used. The $j^{\mathrm{max}}_{\mathrm{b-ID}}$ distributions are shown in Fig. 6. A theoretical $t\bar{t}$ cross section of 7.48 pb is used [37].

VIII. CROSS SECTION DETERMINATION

As shown in Figs. 5 and 6, the MVA output distributions for the $\ell +$ jets and $\ell\ell$ channels allow the discrimination of the $t\bar{t}$ signal contribution and the most dominant background sources. We perform a simultaneous fit of MC templates to the data using the software package COLLIE (A Confidence Level Limit Evaluator) [51] to determine the inclusive $t\bar{t}$ cross section $\sigma(t\bar{t})$.

The combined likelihood includes prior probability densities on systematic uncertainties $\pi(\vec{\theta})$, and is based on the product of likelihoods for the individual channels, each of which is a product over bins of histograms of a particular analysis channel:

$$\mathcal{L}(\vec{s},\vec{b}|\vec{n},\vec{\theta}) \times \pi(\vec{\theta}) = \prod_{i=1}^{N_C}\prod_{j=1}^{N_{\mathrm{bins}}} \mu_{ij}^{n_{ij}} \frac{e^{-\mu_{ij}}}{n_{ij}!} \times \prod_{k=1}^{n_{\mathrm{sys}}} e^{-\theta_k^2/2}. \qquad (1)$$

The first product is over the number of channels (N_C) and the second product is over histogram bins containing n_{ij} events, binned in ranges of the final discriminants used for the individual analyses. The predictions for the bin contents are $\mu_{ij} = s_{ij}(\vec{\theta}) + b_{ij}(\vec{\theta})$ for channel i and histogram bin j, where s_{ij} and b_{ij} represent the expected signal and background in the bin. The predictions μ_{ij} include effects from limited detector resolution and efficiency, including those

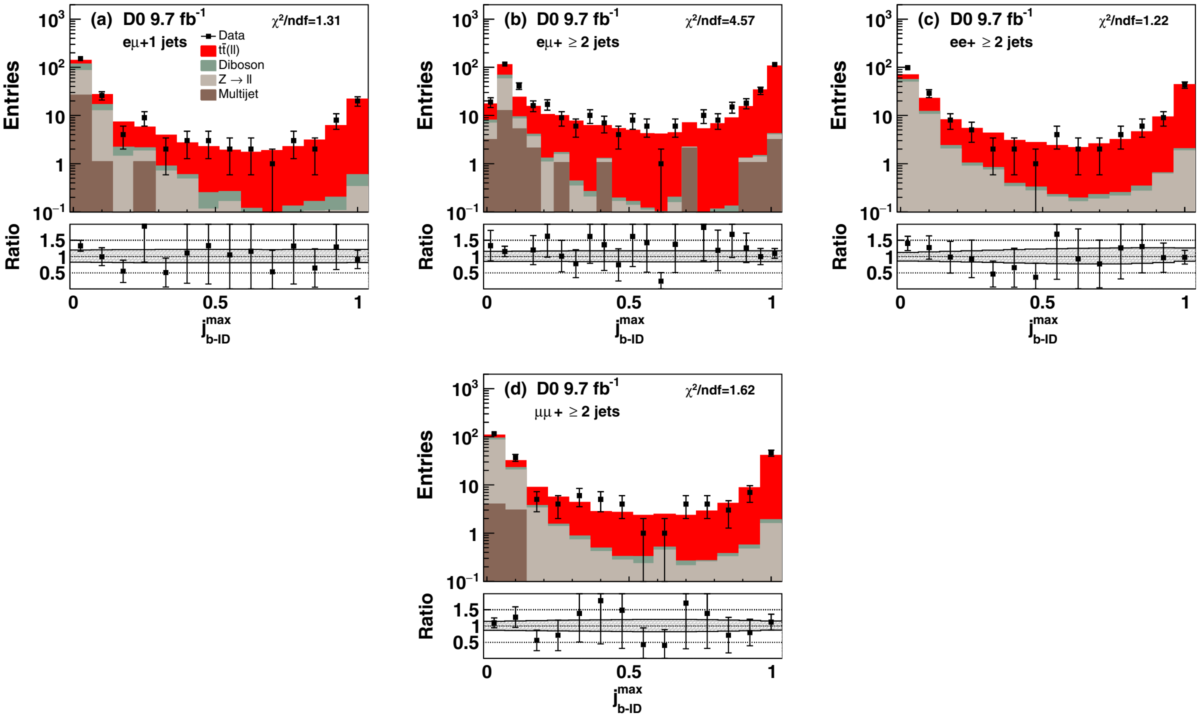

FIG. 6. The pre-fit MVA output distributions (using the theoretical $t\bar{t}$ cross section and $m_t = 172.5$ GeV) of the b-ID MVA given by the jet with the maximum value, $j^{\mathrm{max}}_{\mathrm{b-ID}}$, for (a) $e\mu$ events with exactly one jet, (b) $e\mu$ events with at least two jets, (c) ee events with at least two jets, and (d) $\mu\mu$ events with at least two jets. Statistical uncertainties of the data are shown and the pre-fit systematic uncertainties are indicated by the hashed band in the bottom panel of the histogram. The χ^2/ndf values take statistical and systematic uncertainties into account.

from trigger and selection efficiencies and for the kinematic and geometric acceptance.

Systematic uncertainties are parametrized by the dependence of s_{ij} and b_{ij} on $\vec{\theta}$. Each of the n_{sys} components of $\vec{\theta}$, θ_k, corresponds to a single independent source of systematic uncertainty scaled by its standard deviation, and each parameter may affect the predictions of several sources of signal and background in different channels, thus accounting for correlations. For the combination of the combined MVA in the $\ell +$jets channel with the b-ID MVA in the $\ell\ell$ channel using COLLIE systematic uncertainties are either assumed to be fully correlated or not correlated (see Sec. IX).

COLLIE models nuisance parameters using a Gaussian prior probability density function specified by ±1 standard deviation of the systematic uncertainty in question [see Eq. (1)]. For asymmetric uncertainties, two half-Gaussian functions model separately the positive and negative parts of the nuisance parameters. In the log-likelihood profile fit, the nuisance parameters and the cross section are simultaneously fitted. Hence, sources of systematic uncertainties not only contribute to the final cross section uncertainty, but also shift the fitted cross section value. Since the simultaneous fit is constrained by data it also provides a reduction of the impact of the different systematic uncertainty sources.

The central value of the COLLIE fit provides a scale factor that is applied to the expected number of signal events using the theoretical $t\bar{t}$ cross section. The scaled number of signal events, N^{signal}, is preferred by the data and the systematic uncertainties. To determine $\sigma_{t\bar{t}}$ for the full phase space of $t\bar{t}$ production we correct N^{signal} for the detector efficiency and acceptance, the branching ratio and the integrated luminosity.

IX. SYSTEMATIC UNCERTAINTIES

Systematic uncertainties are assessed by varying the values of a specific parameter in the modeling of the data, and determining the effect on the distributions or MC templates of the combined MVA or the b-ID MVA. Compared to the earlier D0 measurement [3] we employ a more refined strategy for systematic uncertainties including the newly added hadronization uncertainty. Unless otherwise stated, the magnitude of the parameter modifications is obtained from alternative calibrations of the MC simulation. Each of the modified MVA distributions is used to determine the effect of systematic uncertainties. As described in Sec. VIII all nuisance parameters are fitted simultaneously with the nominal MVA distributions to measure the $t\bar{t}$ production cross section. Systematic uncertainties are constrained by the data and are minimized since

TABLE III. Sources of grouped pre-fit systematic uncertainties for the $t\bar{t}$ cross section measurement assuming the theoretical $t\bar{t}$ cross section of 7.48 pb [37] and $m_t = 172.5$ GeV. The systematic uncertainty in pb from each source on the inclusive cross section is given for the $\ell +$ jets and the $\ell\ell$ channels. The column denoted as "Type" refers to a systematic uncertainty affecting the shape and normalization *S* or only the normalization *N* of a MVA distribution. The numbers presented for shape-dependent uncertainties represent averages across the entire set of distributions and all samples. The term "n.a." is used where a systematic uncertainty is not applicable for a given decay channel.

Source of uncertainty	$\delta_{\ell+\mathrm{jets}}$, pb	Type	$\delta_{\ell\ell}$, pb	Type
Signal modeling				
Signal generator	±0.86	*S*	±0.28	*S*
Hadronization	±0.59	*S*	±0.29	*S*
Color reconnection	±0.21	*S*	±0.08	*S*
ISR/FSR variation	±0.07	*S*	±0.04	*S*
PDF	±0.20	*S*	±0.07	*S*
Detector modeling				
Jet modeling & ID	±0.33	*S*	±0.34	*S*
b-jet modeling & ID	±0.19	*S*	±0.56	*S*
Lepton modeling & ID	±0.23	*S*	±0.31	*N*
Trigger efficiency	±0.06	*N*	±0.07	*N*
Luminosity[a]	±0.32	*N*	±0.32	*N*
Sample Composition				
MC cross sections	±0.02	*N*	±0.12	*N*
Z/W p_T reweighting	±0.03	*S*	±0.28	*S*
Multijet contribution	±0.26	*S*	±0.13	*S*
$Z/\gamma^* +$ jets SF	±0.09	*S*	±0.12	*S*
$W +$ jets HF SF	±0.41	*S*	n.a.	n.a.
$W +$ jets LP SF	±0.16	*S*	n.a.	n.a.
MC statistics	±0.01	S	±0.10	*S*

[a] To prevent constraining the luminosity uncertainty by data, we do not assign the luminosity uncertainty to the $W +$ jets and multijet contribution.

we use the full shape information of the MVA templates. A further reduction of correlated systematic uncertainties is achieved when combining the $\ell +$ jets and $\ell\ell$ decay channels, since systematic uncertainties are then cross-calibrated.

In total we assign 39 ($\ell +$ jets channel), 37 ($\ell\ell$ channel), and 53 (combination) individual systematic uncertainties as discussed below for the decay channels. The pre-fit systematic uncertainties are summarized in Table III, whereas the post-fit effects of the systematic uncertainties are summarized in Table IV. We group systematic uncertainties addressing a similar object, e.g. jet-related ones, into a combined source of systematic uncertainty.

TABLE IV. Sources of grouped post-fit systematic uncertainties for the $t\bar{t}$ cross section measurement. Owing to the complexity of the correlations among the systematic uncertainties, we only show here the symmetrized uncertainties. For the top quark signal and background contributions we assume $m_t = 172.5$ GeV. For each group, the systematic uncertainty on the inclusive cross section is given for the $\ell +$ jets, $\ell\ell$ and combined measurement. The last column shows the shift in pb in the combined inclusive cross section due to a particular group. A shift of 0.00 pb indicates a shift of 0.004 pb or less. The total uncertainty is provided by the nominal fit, when including all individual sources of systematic uncertainties, and denoted as "central COLLIE." For comparison only we also provide the combined systematic uncertainty (quadratic sum) of the grouped post-fit systematic uncertainties. Due to correlations between the systematic uncertainties, that value differs from the total systematic uncertainty of the nominal fit.

Source of uncertainty	$\delta_{\ell+\mathrm{jets}}$, pb	$\delta_{\ell\ell}$, pb	$\delta_{\mathrm{comb.}}$, pb	Shift, pb
Signal modeling				
Signal generator	±0.21	±0.05	±0.17	+0.08
Hadronization	±0.26	±0.33	±0.25	+0.12
Color reconnection	±0.08	±0.05	±0.09	+0.02
ISR/FSR variation	±0.08	±0.04	±0.06	−0.05
PDF	±0.04	±0.03	±0.02	−0.01
Detector modeling				
Jet modeling & ID	±0.11	±0.08	±0.04	+0.07
b-jet modeling & ID	±0.27	±0.26	±0.23	−0.15
Lepton modeling & ID	±0.20	±0.26	±0.17	−0.11
Trigger efficiency	±0.32	±0.08	±0.16	+0.01
Luminosity	±0.30	±0.30	±0.27	+0.10
Sample Composition				
MC cross sections	±0.07	±0.13	±0.09	+0.01
Multijet contribution	±0.11	±0.02	±0.10	+0.10
$W +$ jets scale factor	±0.21	±0.01	±0.15	−0.50
$Z/\gamma^* +$ jets scale factor	±0.07	±0.11	±0.12	+0.12
MC statistics	±0.01	±0.01	±0.02	+0.00
Total systematic uncertainty (quadratic sum)	±0.70	±0.64	±0.60	
Total systematic uncertainty (central COLLIE)	±0.67	±0.73	±0.55	

A. The $\ell +$ jets channel

In the following we describe the sources of systematic uncertainties studied in the $\ell +$ jets channel. As discussed above, each source of systematic uncertainty yields a modified discriminant distribution, which is parametrized with a nuisance parameter (see Sec. VIII). We assign an uncertainty on the shape, but not on the normalization, of the $W +$ jets and multijet contribution (see Sec. VI A). In particular the trigger and luminosity uncertainties affecting the normalization are not assigned to the $W +$ jets and multijet contribution, and consequently the luminosity uncertainty cannot be constrained by data.

1. Signal modeling

The effect of an alternative signal model for $t\bar{t}$ production is estimated by comparing $t\bar{t}$ events generated with MC@NLO + HERWIG to those from ALPGEN + HERWIG. Comparing ALPGEN + PYTHIA to ALPGEN + HERWIG, we estimate the effect of hadronization uncertainties. Additional uncertainties on signal arise from color reconnection (CR), and initial- and final-state radiation (ISR/FSR) producing additional jets. The effect of CR is determined by comparing identical ALPGEN events interfaced to PYTHIA with two different tunes, Perugia 2011 and Perugia 2011NOCR [52], which either include color reconnection effects (Perugia 2011) or not (Perugia 2011NOCR). The effect of ISR/FSR is determined by modifying the factorization and renormalization scale implemented in the MC. More details can be found in Ref. [53].

2. Parton distribution functions

The uncertainty on the cross sections due to the uncertainty on PDFs is estimated following the procedure of Ref. [35] by reweighting the MC simulation according to each of the 20 pairs of error eigenvectors of the CTEQ6M PDF.

3. Detector modeling

Uncertainties on the modeling of the detector include uncertainties on trigger efficiency, lepton identification, and b-quark identification. The identification efficiencies for b, c, light quarks (u, d, s), and gluons in MC simulations are calibrated using dijet data [54], and variations within the calibration uncertainty are used to determine the systematic uncertainty due to b-quark identification. Additional uncertainties arise from track multiplicity requirements on the selected jets in the identification of b quarks.

The measurement of the $t\bar{t}$ cross section and the subsequent extraction of the top quark pole mass relies on a precise knowledge of normalization uncertainties. Hence, this measurement is the first measurement in D0 employing the reduced systematic uncertainty on the luminosity measurement of 4.3% [20,21]. We use an auxiliary data sample where no cut is made on the primary vertex position in z to verify that negligible uncertainty arises for the $|z_{\mathrm{PV}}| < 60$ cm requirement used in this analysis. Other instrumental uncertainties from modeling the detector arise from the calibration of the jet energy, resolution, and efficiency.

4. Sample composition

Uncertainties in the composition of the selected events arise from $s_{\mathrm{fit}}^{\mathrm{WHF}}$ and $s_{\mathrm{fit}}^{\mathrm{WLF}}$ used for $W+$jets events, the assumed $t\bar{t}$ cross section, single top quark and diboson cross sections, and the estimate of the contributions from misidentified leptons. As introduced in Sec. VI, we determine an initial sample composition from a simultaneous fit to the MVA distribution in the $\ell+2$jets, $\ell+3$jets and $\ell+\geq 4$jets samples. For this initial sample composition we fit $s_{\mathrm{fit}}^{\mathrm{WHF}}$ and $s_{\mathrm{fit}}^{\mathrm{WLF}}$ assuming an uncertainty of 5% on the normalization of the $t\bar{t}$ processes. This initial sample composition is only used to determine a systematic uncertainty on the contribution of $W+$jets processes. From the fit we derive a systematic uncertainty of $^{+3.5}_{-1.8}\%$ on the normalization of the $Wlp+$jets and $^{+17}_{-23}\%$ on the normalization of the $Wc\bar{c}+$jets and $Wb\bar{b}+$jets processes. The statistical uncertainties on these processes are negligible. An uncertainty of 25% on the Z/γ^*+jets cross section is assigned. The uncertainty on the single top quark cross sections is 12.6%, taken from varying the factorization and renormalization scales simultaneously by factors of 2 and 0.5. An uncertainty of 7% on the diboson cross sections is assigned, corresponding to half the difference between the LO and NLO predictions. The uncertainties on the single top quark and diboson contributions are labeled “MC cross sections” in the corresponding tables. The uncertainties on the data-driven method of estimating MJ background and its kinematic dependences, mostly due to the uncertainties on the selection rates of true and false lepton candidates, are 40% in the $\mu+$jets and 25% in the $e+$jets sample (including statistical components). These uncertainties are estimated by varying the contribution of $Wc\bar{c}+$jets, $Wb\bar{b}+$jets, $Zc\bar{c}+$jets and $Zb\bar{b}+$jets by ±20%, the $t\bar{t}$ contribution by ±10%, and then comparing the fake and true signal rates in different variables (quoting the largest difference as additional parametrization uncertainty) [46].

B. The $\ell\ell$ channel

In the following we describe the sources of systematic uncertainties studied in the $\ell\ell$ channel, which are mostly similar to those in the $\ell+$jets channel. As discussed above, each source of systematic uncertainty yields a modified discriminant distribution of the b-ID MVA and a nuisance parameter is used in the fit to determine the $t\bar{t}$ production cross section in the $\ell\ell$ channel. Uncertainties on the sample composition only apply to certain sample contributions. Uncertainties due to common sources are assumed to be 100% correlated between the $\ell+$jets channel and the $\ell\ell$ channel unless otherwise specified.

1. Signal modeling

The same sources of systematic uncertainties for the modeling of the signal as in the $\ell+$jets decay channel are considered for the $\ell\ell$ channel as well.

2. Parton distribution functions

The uncertainty on the cross sections due to the uncertainty on PDFs is estimated following the same procedure as in the $\ell+$jets case.

3. Detector modeling

The assigned uncertainties related to the modeling of the detector are the same as the ones assigned in the $\ell+$jets channel and include uncertainties on the efficiencies of electron and muon identification, uncertainties on trigger

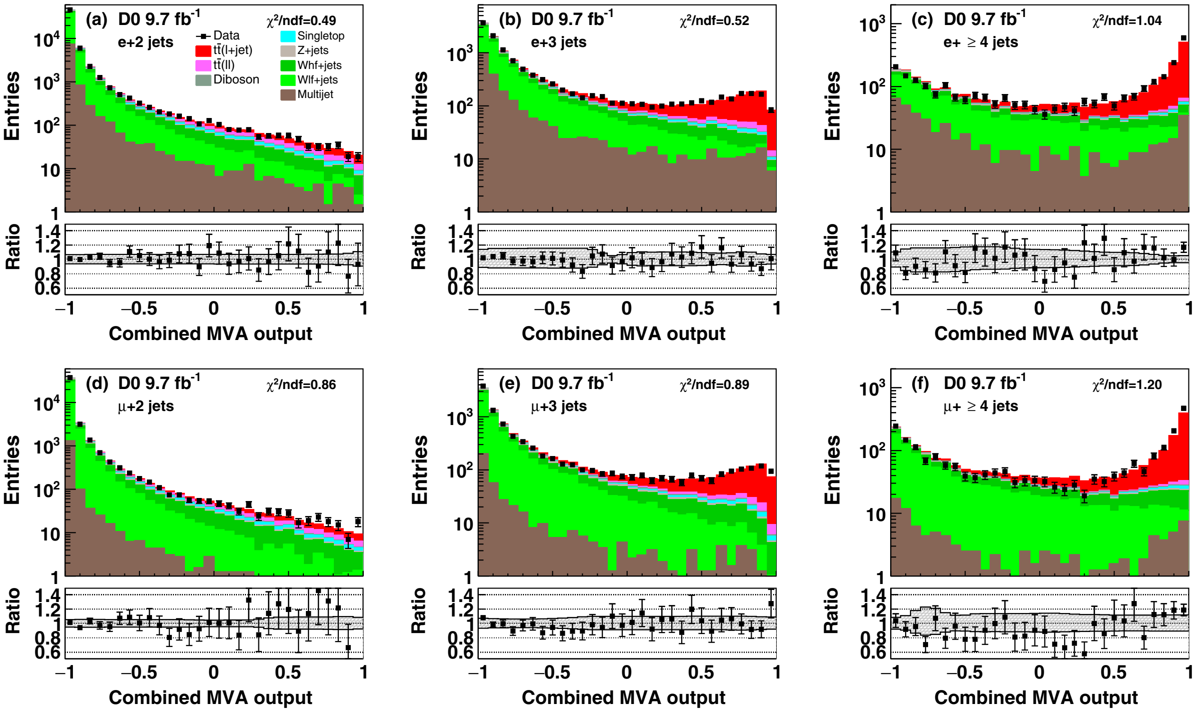

FIG. 7. Post-fit output distributions of the combined MVA discriminant using the measured combined $t\bar{t}$ cross section and $m_t = 172.5$ GeV for the $e+$ two, three or four or more jets [panels (a)–(c)], and for the $\mu+$ two, three or four or more jets [panels (d)–(f)]. Statistical uncertainties of the data are shown and the post-fit systematic uncertainties are indicated by the hashed band in the bottom panel of the histogram. The χ^2/ndf values take statistical and systematic uncertainties into account.

efficiencies, the uncertainty in jet energy scale, jet energy resolution, jet identification efficiency, and b-quark jet tagging efficiency. The $\ell+$jets and $\ell\ell$ event selection ensures that the samples are dominantly orthogonal. Hence, we assume the uncertainties arising from modeling of the trigger to be not correlated between the $\ell+$jets and $\ell\ell$ channels.

4. Sample composition

We estimate the uncertainty on the instrumental background contribution in the $\ell\ell$ channel by changing the normalization of that background by ±1 standard deviation of its uncertainty. It includes both the statistical uncertainty on the sample used to derive the normalization and the systematic uncertainty in the lepton misidentification rate. Uncertainties from $Z/\gamma^* +$jets and diboson production are taken into account with the same assumptions as in the $\ell+$jets case. Uncertainties arising from the determination of the MJ background are assumed to be not correlated between the $\ell+$jets and $\ell\ell$ channel.

X. CROSS SECTION RESULTS

The result of the measurement in the $\ell+$jets channel using the combined MVA method is

$$\sigma_{t\bar{t}} = 7.33 \pm 0.14(\mathrm{stat})^{+0.71}_{-0.61}(\mathrm{syst})\ \mathrm{pb},$$

with a relative total uncertainty of 9.2%. For the $\ell\ell$ decay channel we employ the MVA b-jet method and measure

$$\sigma_{t\bar{t}} = 7.58 \pm 0.35(\mathrm{stat})^{+0.69}_{-0.58}(\mathrm{syst})\ \mathrm{pb},$$

with a relative total uncertainty of 9.6%.

The combination of the $t\bar{t}$ cross section is carried out by a simultaneous COLLIE fit of the combined MVA and the MVA b-jet discriminant distributions in the $\ell+$jets and $\ell\ell$ channels. For a top quark mass of 172.5 GeV we measure

$$\sigma_{t\bar{t}} = 7.26 \pm 0.13(\mathrm{stat})^{+0.57}_{-0.50}(\mathrm{syst})\ \mathrm{pb},$$

which corresponds to a relative total uncertainty of 7.6%. For the combined $\ell+$jets and $\ell\ell$ $t\bar{t}$ cross section measurement we profile the systematic uncertainties by employing the MVA discriminant distributions simultaneously in both channels. The combined $t\bar{t}$ cross section does not coincide with the weighted average of the individual $\ell+$jets and $\ell\ell$ results, which is attributed to the effect of correlations of systematic uncertainties between both channels.

Table IV summarizes the post-fit systematic uncertainties on the $t\bar{t}$ cross section in the $\ell+$jets and $\ell\ell$ decay channels and for the combination. The impact of these sources is estimated by removing or including the corresponding "group" of individual sources from the fit. The total uncertainty is provided by the nominal fit, when including all individual sources of systematic uncertainties,

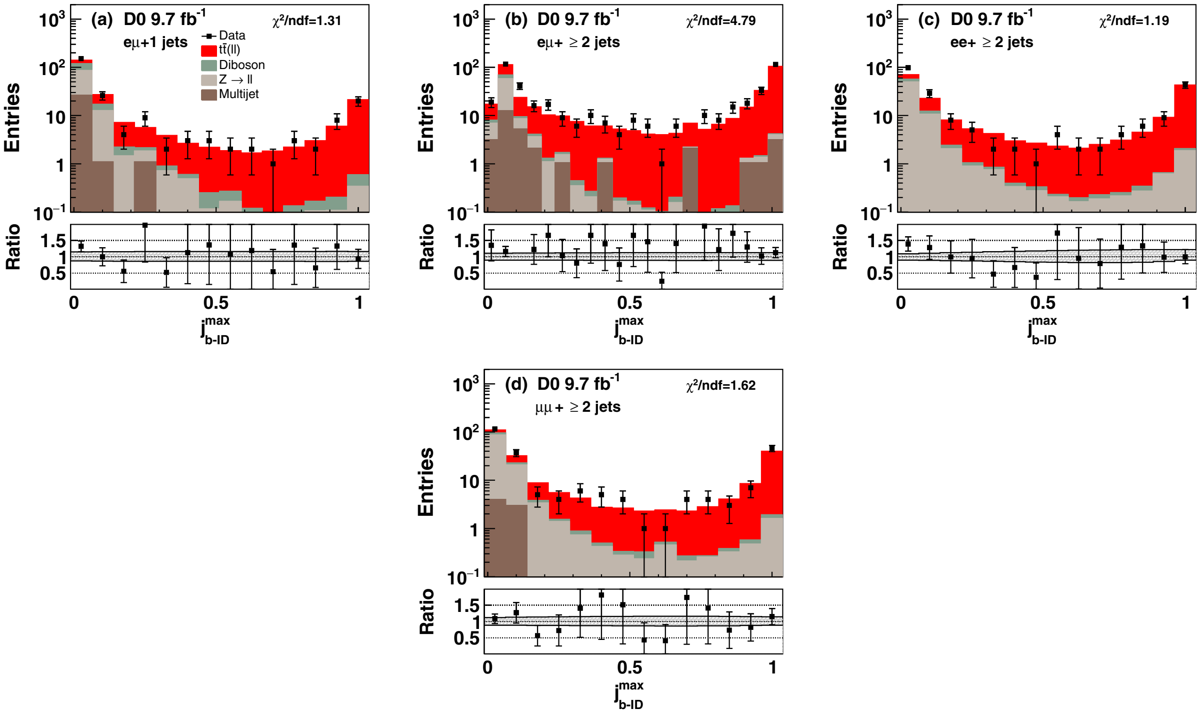

FIG. 8. The post-fit MVA output distributions (assuming $m_t = 172.5$ GeV) of $j^{\max}_{\text{b-ID}}$ for (a) $e\mu$ events with exactly one jet, (b) $e\mu$ events with at least two jets, (c) ee events with at least two jets, and (d) $\mu\mu$ events with at least two jets are shown. Statistical uncertainties of the data are shown and the post-fit systematic uncertainties are indicated by the hashed band in the bottom panel of the histogram. The χ^2/ndf values take statistical and systematic uncertainties into account.

and denoted as "central COLLIE" in Table IV. For comparison only we also provide the quadratic sum of the groups of systematic uncertainties. Due to correlations being different between the groups and all the individual systematic uncertainties, that value differs from the total systematic uncertainty of the nominal fit. In addition, we provide the "Shift" in units of pb, which refers to shifts on the combined inclusive cross section due to a particular source of systematic uncertainty relative to the central value of the combined $t\bar{t}$ cross section.

Figure 7 shows the post-fit MVA combined discriminant distributions for the $\ell +$jets channel using the combined $t\bar{t}$ cross section. Similarly Fig. 8 shows the post-fit MVA b-ID discriminant distribution for the $\ell\ell$ channel using the combined $t\bar{t}$ cross section. This result is consistent with and supersedes our earlier measurement using 5.3 fb^{-1} of data [3]. The inclusive $t\bar{t}$ production cross section is in agreement with the fully resummed next-to-next-to-leading logarithm at NNLO QCD calculation (see Sec. IV) of $\sigma^{\text{res}}_{\text{tot}} = 7.35^{+0.23}_{-0.27}(\text{scale} + \text{pdf})$ pb.

XI. TOP QUARK POLE MASS

Table V presents the measured combined inclusive $t\bar{t}$ cross section as a function of the top quark mass. For each top quark mass point shown a separate combined log-likelihood fit of the $\ell +$jets and $\ell\ell$ channel MVA discriminant inputs was performed, as was done for the mass point of 172.5 GeV. The measured $t\bar{t}$ cross section only changes by 0.7% for a change of 1 GeV in the assumed top quark mass. Systematic uncertainties of the $t\bar{t}$ contribution are taken from the 172.5 GeV case and assigned to other masses as a relative systematic uncertainty of the same size.

Figure 9 shows the measured and theoretical mass dependence of the inclusive $t\bar{t}$ production cross section as provided by TOP++ [41]. We parametrize the experimentally measured dependence with a fourth-order

TABLE V. The measured combined inclusive $t\bar{t}$ cross section as a function of the top quark MC mass with statistical and systematic uncertainties given separately.

Top quark mass [GeV]	Cross section $\sigma(t\bar{t})$[pb]
150	$9.70 \pm 0.16(\text{stat})^{+0.73}_{-0.67}(\text{syst})$
160	$8.25 \pm 0.14(\text{stat})^{+0.63}_{-0.57}(\text{syst})$
165	$7.46 \pm 0.13(\text{stat})^{+0.58}_{-0.51}(\text{syst})$
170	$7.55 \pm 0.13(\text{stat})^{+0.58}_{-0.55}(\text{syst})$
172.5	$7.26 \pm 0.12(\text{stat})^{+0.57}_{-0.50}(\text{syst})$
175	$7.28 \pm 0.12(\text{stat})^{+0.54}_{-0.49}(\text{syst})$
180	$6.86 \pm 0.12(\text{stat})^{+0.53}_{-0.47}(\text{syst})$
185	$6.50 \pm 0.11(\text{stat})^{+0.50}_{-0.43}(\text{syst})$
190	$6.70 \pm 0.11(\text{stat})^{+0.60}_{-0.47}(\text{syst})$

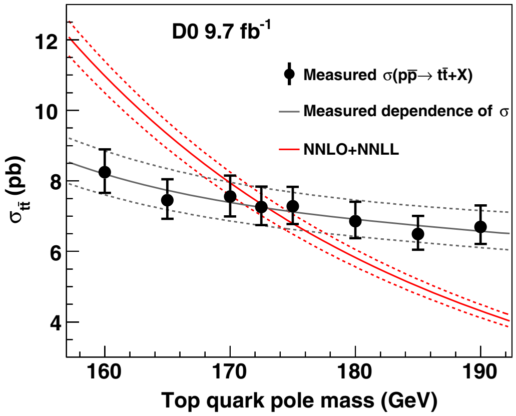

FIG. 9. The measured $t\bar{t}$ production cross section dependence on the top quark mass (points) parametrized by a quartic function (solid black line) and compared to the dependence provided by the NNLO pQCD calculation TOP++ [41], which implements pQCD calculations according to Ref. [38].

polynomial function to the individual cross section measurements at the mass points reported in Table V. There is negligible change if a cubic function is chosen. Uncertainties on the measured values include the statistical and systematic uncertainties discussed in Sec. IX and are indicated by the dotted lines. Theoretical uncertainties include those from the variation of the renormalization and factorization scales by a factor of 2 and PDF uncertainties [40] taken from the MSTW2008 NNLO PDF set. These are added in quadrature and indicated by the dotted lines surrounding the central theoretical prediction.

To determine the top quark pole mass from the inclusive $t\bar{t}$ cross section following the method in Ref. [55], we extract the most probable m_t value and uncertainty by employing a normalized joint-likelihood function, which takes into account the total experimental uncertainty, the theoretical uncertainties on the renormalization and factorization scales, and the PDF uncertainties. Employing the quartic parametrization and the theory predictions at NNLO pQCD we obtain

$$m_t = 172.8 \pm 1.1(\text{theo})^{+3.3}_{-3.1}(\text{exp})\ \text{GeV}, \quad \text{or}$$
$$m_t = 172.8^{+3.4}_{-3.2}(\text{tot})\ \text{GeV}.$$

The experimental uncertainties dominate the precision of the determination. The precision of this determination is 1.9%, and represents the most precise determination of the top quark pole mass from the inclusive $t\bar{t}$ cross section at the Tevatron. This supersedes our previous determination which had a precision of 3% [55].

XII. CONCLUSIONS

The inclusive $t\bar{t}$ production cross section has been measured combining the lepton + jets and dilepton top quark decay channels based on the full Tevatron data set at $\sqrt{s} = 1.96$ TeV. We performed a simultaneous log-likelihood fit to profile systematic uncertainties and, for a top quark mass of 172.5 GeV, we measured a combined $t\bar{t}$ cross section of

$$\sigma_{t\bar{t}} = 7.26 \pm 0.13(\text{stat})^{+0.57}_{-0.50}(\text{syst})\ \text{pb},$$

which corresponds to a relative uncertainty of 7.6%. This result and the measured inclusive cross sections per decay channel are in good agreement with predictions by QCD.

We employed the dependence of the theoretical cross section on the top mass, to determine a pole mass of the top quark of

$$m_t = 172.8^{+3.4}_{-3.2}(\text{tot})\ \text{GeV}.$$

The uncertainty corresponds to a precision of 1.9% and represents the most precise determination of the top quark pole mass at the Tevatron.

ACKNOWLEDGMENTS

We thank Vladimir Shiltsev for enlightening discussions. We thank the staffs at Fermilab and collaborating institutions, and acknowledge support from the Department of Energy and National Science Foundation (United States of America); Alternative Energies and Atomic Energy Commission and National Center for Scientific Research/National Institute of Nuclear and Particle Physics (France); Ministry of Education and Science of the Russian Federation, National Research Center "Kurchatov Institute" of the Russian Federation, and Russian Foundation for Basic Research (Russia); National Council for the Development of Science and Technology and Carlos Chagas Filho Foundation for the Support of Research in the State of Rio de Janeiro (Brazil); Department of Atomic Energy and Department of Science and Technology (India); Administrative Department of Science, Technology and Innovation (Colombia); National Council of Science and Technology (Mexico); National Research Foundation of Korea (Korea); Foundation for Fundamental Research on Matter (The Netherlands); Science and Technology Facilities Council and The Royal Society (United Kingdom); Ministry of Education, Youth and Sports (Czech Republic); Bundesministerium für Bildung und Forschung (Federal Ministry of Education and Research) and Deutsche Forschungsgemeinschaft (German Research Foundation) (Germany); Science Foundation Ireland (Ireland); Swedish Research Council (Sweden); China Academy of Sciences and National Natural Science Foundation of China (China); and Ministry of Education and Science of Ukraine (Ukraine).

APPENDIX: VARIABLES SELECTED FOR THE COMBINED MVA DISCRIMINANT

Depending on the number of jets in an event, we select at least 24 variables for the combined MVA to measure the $t\bar{t}$

production cross section in the $\ell+$jets decay channel. The list given below is sorted according to the ranking in terms of separation power as provided by the BDTG method.

(1) $j^{\mathrm{max}}_{\mathrm{b-ID}}$: The maximum output value of the MVA b-jet discriminant of all jets in an event.
(2) H^3_T: The scalar sum of transverse momenta of jets excluding the leading and subleading jets.
(3) $H^{2.0}_T$: The scalar sum of transverse momenta of jets satisfying $|\eta| < 2.0$.
(4) j^1_b: The $b-\mathrm{ID}$ MVA output value of the leading jet.
(5) Centrality $\mathcal{C}$: Ratio of the scalar sum of the transverse momentum of all jets to the energy of all jets.
(6) H_T: The scalar sum of the transverse momenta of all jets, the lepton and $\not{E}_T$.
(7) $p^{\mathrm{j}_i}_T$: The transverse momenta of the individual jets i.
(8) j^2_b: The $b-\mathrm{ID}$ MVA value of the second leading jet.
(9) H^{ℓ}_T: The scalar sum of the transverse momenta of all jets and the lepton.
(10) Sphericity $\mathcal{S}$: Diagonalizing the normalized quadratic momentum tensor $\mathcal{M}$ yields three eigenvalues λ_i [3], with $\lambda_1 > \lambda_2 > \lambda_3$. The sphericity is defined as $\mathcal{S} = \frac{3}{2}(\lambda_2 + \lambda_3)$ and reflects the degree of isotropy of an event.
(11) $m(t\bar{t})$: The invariant mass of the $t\bar{t}$ pair. The energy of the neutrino is determined by constraining the invariant mass of the lepton and vector $\not{E}_T$ (as the neutrino) to the mass of the W boson. Of the two possible solutions for the longitudinal momentum of the neutrino, we use the one with the smallest absolute value.
(12) η^{j_1}: The rapidity of the leading jet.
(13) $\Delta R(j^1, j^2)$: The separation in the distance R between the leading and second leading jet.
(14) p^W_T: The transverse momentum of the reconstructed W boson which decays hadronically.
(15) $M^{\mathrm{j}_2\nu\ell}_T$: The transverse mass of the system consisting of the second leading jet, the neutrino, and the lepton.
(16) Aplanarity $\mathcal{A}$: The aplanarity is defined as $3/2$ times the momentum tensor eigenvalue λ_3.
(17) $\Delta R(j^1, j^{i\geq 3})$: The separation in the distance R between the leading and each jet beyond the second leading jet.
(18) m_{jet}: The invariant mass of the jets.
(19) M^{jet}_T: The transverse mass of the first two leading jets.
(20) $M_{\mathrm{j}_2\nu\ell}$: The invariant mass of the system consisting of the second leading jet, the neutrino, and the lepton.
(21) $\Delta\phi(\ell, \not{E}_T)$: The separation in azimuth between the lepton and the direction of $\not{E}_T$.
(22) $\not{E}_T$: Missing transverse momentum.
(23) η^{lepton}: The rapidity of the lepton.
(24) $\Delta\phi(j^1, j^i)$: The minimum separation in azimuth between the leading and any other jet.
(25) $\not{E}_T{}^{\mathrm{perp}}$: Component of the missing transverse momentum perpendicular to the direction of the lepton.

---

[1] F. Abe *et al.* (CDF Collaboration), Observation of top quark production in $p\bar{p}$ collisions, Phys. Rev. Lett. **74**, 2626 (1995).
[2] S. Abachi *et al.* (D0 Collaboration), Observation of the top quark, Phys. Rev. Lett. **74**, 2632 (1995).
[3] V. M. Abazov *et al.* (D0 Collaboration), Measurement of the top quark pair production cross section in the lepton + jets channel in proton-antiproton collisions at $\sqrt{s} = 1.96$ TeV, Phys. Rev. D **84**, 012008 (2011).
[4] F. Abe *et al.* (CDF Collaboration), Measurement of the top-quark pair-production cross section in events with two leptons and bottom-quark jets using the full CDF data set, Phys. Rev. D **88**, 091103 (2013).
[5] S. Chatrchyan *et al.* (CMS Collaboration), Measurement of the $t\bar{t}$ production cross section in the dilepton channel in $p\overline{p}$ collisions at $\sqrt{s} = 8$ TeV, J. High Energy Phys. 02 (2014) 024.
[6] G. Aad *et al.* (ATLAS Collaboration), Measurement of the top pair production cross section in 8 TeV proton-proton collisions using kinematic information in the lepton + jets final state with ATLAS, Phys. Rev. D **91**, 112013 (2015).
[7] R. Aaij *et al.* (LHCb Collaboration), First observation of top quark production in the forward region, Phys. Rev. Lett. **115**, 112001 (2015).
[8] V. M. Abazov *et al.* (D0 Collaboration), Precision measurement of the top-quark mass in lepton + jets final states, Phys. Rev. Lett. **113**, 032002 (2014).
[9] V. M. Abazov *et al.* (CDF and D0 Collaborations), Combination of the top-quark mass measurements from the Tevatron collider, Phys. Rev. D **86**, 092003 (2012), updated in arXiv:1407.2682.
[10] S. Weinzierl, Precision of the top mass, in *Proceedings of the 50th Rencontres de Moriond on EW Interactions and Unified Theories, La Thuile, Italy, March 14-21, 2015*, edited by E. Augé, J. Dumarchez, and J. T. T. Vân (ARSIF, Paris, 2015).
[11] K. Kondo, Dynamical likelihood method for reconstruction of events with missing momentum. 1: Method and toy models, J. Phys. Soc. Jpn. **57**, 4126 (1988).
[12] R. M. Neal, *Bayesian Learning for Neural Networks* (Springer-Verlag, Berlin, 1996).
[13] L. Breiman, J. Friedman, C. J. Stone, and R. A. Olshen, *Classification and Regression Trees* (Wadsworth, Stamford, 1984).

[14] A. Hoecker, P. Speckmayer, J. Stelzer, J. Therhaag, E. von Toerne, and H. Voss, TMVA-toolkit for multivariate data analysis, *Proc. Sci.*, ACAT2007 (2007) 040.

[15] V. M. Abazov *et al.* (D0 Collaboration), Improved b quark jet identification at the D0 experiment, Nucl. Instrum. Methods Phys. Res., Sect. A **763**, 290 (2014).

[16] V. M. Abazov *et al.* (D0 Collaboration), The upgraded D0 detector, Nucl. Instrum. Methods Phys. Res., Sect. A **565**, 463 (2006).

[17] S. N. Ahmed *et al.*, The D0 silicon microstrip tracker, Nucl. Instrum. Methods Phys. Res., Sect. A **634**, 8 (2011).

[18] R. Angstadt *et al.*, The layer 0 inner silicon detector of the D0 experiment, Nucl. Instrum. Methods Phys. Res., Sect. A **622**, 298 (2010).

[19] V. M. Abazov *et al.* (D0 Collaboration), The muon system of the Run II D0 detector, Nucl. Instrum. Methods Phys. Res., Sect. A **552**, 372 (2005).

[20] T. Andeen *et al.*, The D0 experiment's integrated luminosity for Tevatron run IIa, Report No. FERMILAB-TM-2365 (2007).

[21] B. C. K. Casey *et al.*, The D0 Run IIb luminosity measurement, Nucl. Instrum. Methods Phys. Res., Sect. A **698**, 208 (2013).

[22] M. Abolins *et al.*, Design and implementation of the new D0 level-1 calorimeter trigger, Nucl. Instrum. Methods Phys. Res., Sect. A **584**, 75 (2008).

[23] V. M. Abazov *et al.* (D0 Collaboration), Electron and photon identification in the D0 experiment, Nucl. Instrum. Methods Phys. Res., Sect. A **750**, 78 (2014).

[24] V. M. Abazov *et al.* (D0 Collaboration), Muon reconstruction and identification with the Run II D0 detector, Nucl. Instrum. Methods Phys. Res., Sect. A **737**, 281 (2014).

[25] G. Blazey *et al.*, Run II jet physics, arXiv:hep-ex/0005012.

[26] V. M. Abazov *et al.* (D0 Collaboration), Jet energy scale determination in the D0 experiment, Nucl. Instrum. Methods Phys. Res., Sect. A **763**, 0 (2014).

[27] R. Brun and F. Carminati, CERN Program Library Long Writeup W5013, 1993 (unpublished).

[28] S. Frixione and B. R. Webber, Matching NLO QCD computations and parton shower simulations, J. High Energy Phys. 06 (2002) 029; S. Frixione, P. Nason, and B. R. Webber, Matching NLO QCD and parton showers in heavy flavour production, J. High Energy Phys. 08 (2003) 007.

[29] M. L. Mangano, M. Moretti, F. Piccinini, R. Pittau, and A. D. Polosa, ALPGEN, a generator for hard multiparton processes in hadronic collisions, J. High Energy Phys. 07 (2003) 001.

[30] G. Corcella, I. G. Knowles, G. Marchesini, S. Moretti, K. Odagiri, P. Richardson, M. H. Seymour, and B. R. Webber, HERWIG 6.5: an event generator for hadron emission reactions with interfering gluons (including supersymmetric processes), J. High Energy Phys. 01 (2001) 010.

[31] T. Sjøstrand, S. Mrenna, and P. Skands, PYTHIA 6.4 physics and manual, J. High Energy Phys. 05 (2006) 026.

[32] E. Boos *et al.* (CompHEP Collaboration), CompHEP 4.4—Automatic computations from Lagrangians to events, Nucl. Instrum. Methods Phys. Res., Sect. A **534**, 250 (2004).

[33] A. Pukhov *et al.*, CompHEP—A package for evaluation of Feynman diagrams and integration over multi-particle phase space, User's manual for version 3.3, arXiv:hep-ph/9908288.

[34] J. Pumplin, D. R. Stump, J. Huston, H.-L. Lai, P. Nadolsky, and W.-K. Tung, New generation of parton distributions with uncertainties from global QCD analysis, J. High Energy Phys. 07 (2002) 12.

[35] D. Stump, J. Huston, J. Pumplin, W.-K. Tung, H. L. Lai, S. Kuhlmann, and J. F. Owens, Inclusive jet production, parton distributions, and the search for new physics, J. High Energy Phys. 10 (2003) 46.

[36] K. A. Olive *et al.* (Particle Data Group), Review of particle physics, Chin. Phys. C **38**, 090001 (2014).

[37] S. Moch and P. Uwer, Theoretical status and prospects for top-quark pair production at hadron colliders, Phys. Rev. D **78**, 034003 (2008).

[38] P. Bärnreuther, M. Czakon, and A. Mitov, Percent-level-precision physics at the Tevatron: Next-to-next-to-leading order QCD corrections to $q\bar{q} \to t\bar{t} + X$, Phys. Rev. Lett. **109**, 132001 (2012).

[39] N. Kidonakis, NNNLO soft-gluon corrections for the top-antitop pair production cross section, Phys. Rev. D **90**, 014006 (2014).

[40] A. D. Martin, W. J. Stirling, R. S. Thorne, and G. Watt, Parton distributions for the LHC, Eur. Phys. J. C **63**, 189 (2009).

[41] M. Czakon and A. Mitov, TOP++: a program for the calculation of the top-pair cross-section at hadron colliders, Comput. Phys. Commun. **185**, 2930 (2014).

[42] J. Campell and R. K. Ellis, MCFM for the Tevatron and the LHC, Nucl. Phys. B, Proc. Suppl. **10**, 205 (2010).

[43] V. M. Abazov *et al.* (D0 Collaboration), Measurement of the normalized $Z/\gamma^* \to \mu^+\mu^-$ transverse momentum distribution in $p\bar{p}$ collisions at $\sqrt{s} = 1.96$ TeV, Phys. Lett. B **693**, 522 (2010).

[44] C. Balazs and C. P. Yuan, Soft gluon effects on lepton pairs at hadron colliders, Phys. Rev. D **56**, 5558 (1997).

[45] N. Kidonakis, Single top production at the Tevatron: Threshold resummation and finite-order soft gluon corrections, Phys. Rev. D **74**, 114012 (2006).

[46] V. M. Abazov *et al.* (D0 Collaboration), Measurement of differential $t\bar{t}$ production cross sections in $p\bar{p}$ collisions, Phys. Rev. D **90**, 092006 (2014).

[47] V. M. Abazov *et al.* (D0 Collaboration), Measurement of the asymmetry in angular distributions of leptons produced in dilepton $t\bar{t}$ final states in $p\bar{p}$ collisions at $\sqrt{s} = 1.96$ TeV, Phys. Rev. D **88**, 112002 (2013).

[48] V. M. Abazov *et al.* (D0 Collaboration), Measurement of the $t\bar{t}$ production cross section in $p\bar{p}$ collisions at $\sqrt{s} = 1.96$ TeV using secondary vertex b tagging, Phys. Rev. D **74**, 112004 (2006).

[49] J. H. Friedman, Greedy function approximation: A gradient boosting machine, IMS Reitz Lecture, 1999 (unpublished).

[50] I. M. Chakravarti, R. G. Laha, and J. Roy, *Handbook of Methods of Applied Statistics*, Vol. I (John Wiley & Sons, New York, 1967), p. 392.

[51] V. M. Abazov *et al.* (CDF & D0 Collaborations), Higgs boson studies at the Tevatron, Phys. Rev. D **88**, 052014 (2013).

[52] P. Skands and D. Wicke, Non-perturbative QCD effects and the top mass at the Tevatron, Eur. Phys. J. C **52**, 133 (2007).

[53] V. M. Abazov *et al.* (D0 Collaboration), Precision measurement of the top-quark mass in lepton + jets final states, Phys. Rev. D **91**, 112003 (2015).

[54] V. M. Abazov *et al.* (D0 Collaboration), Precise measurement of the top-quark mass from lepton + jets events at D0, Phys. Rev. D **84**, 032004 (2011).

[55] V. M. Abazov *et al.* (D0 Collaboration), Determination of the pole and $M\overline{S}$ masses of the top quark from the $t\bar{t}$ cross section, Phys. Lett. B **703**, 422 (2011).